Heterogeneous Synaptic Homeostasis: A Novel Mechanism Boosting Information Propagation in the Cortex

Farhad Razi[1,2,✉] **and Belén Sancristóbal**[1]

[1]ELISAVA Barcelona School of Design and Engineering, Universitat de Vic—Universitat Central de Catalunya, Barcelona, Spain
[2]Donders Institute for Brain, Cognition and Behaviour, Radboud University, Nijmegen, The Netherlands

Perceptual awareness of auditory stimuli decreases from wakefulness to sleep, largely due to reduced cortical responsiveness. During wakefulness, neural responses to external stimuli exhibit a broader spatiotemporal propagation pattern compared to deep sleep. A potential mechanism for this phenomenon is the synaptic upscaling of cortical excitatory connections during wakefulness, as posited by the synaptic homeostasis hypothesis. However, we argue that uniform synaptic upscaling alone cannot fully account for this observation. We propose a novel mechanism suggesting that the upscaling of excitatory connections between different cortical areas exceeds that within individual cortical areas during wakefulness. Our computational results demonstrate that the former promotes the transfer of neural responses and information, whereas the latter has diminishing effects. These findings highlight the necessity of heterogeneous synaptic upscaling and suggest the presence of heterogeneity in receptor expression for neuromodulators involved in synaptic modulation along the dendrite.

cortical effective connectivity | heterogeneous synaptic homeostasis | information propagation | wakefulness | NREM sleep

Correspondence: ***farhad.razi@donders.ru.nl***

DRAFT

Introduction

During the sleep-wake cycle (SWC), the capacity of the cerebral cortex to transmit neural signals across cortical areas, known as cortical effective connectivity (1), is higher during wakefulness compared to the deep phases of non-rapid eye movement (NREM) sleep (2–4). However, the precise neural mechanisms underlying this enhanced propagation of neural responses remain largely speculative.

Changes in neuronal and synaptic dynamics across the SWC within neural pathways could alter propagation patterns. Experimental evidence indicates that low concentrations of neuromodulators released from the ascending arousal network (AAN) during sleep (5) modulate neuronal dynamics (6, 7) and synaptic strength (8–10). The characteristic oscillating dynamics of neuronal transmembrane voltage, alternating between active (Up) and silent (Down) states during NREM sleep (6, 7), might interrupt communication between cortical regions (11–14). According to this view, evoked Down states following external perturbations in cortical neurons disrupt long-lasting causal interactions among cortical areas during NREM sleep. However, direct experimental evidence supporting this claim remains elusive, and certain empirical observations challenge it as the sole reason for altered cortical effective connectivity during sleep.

For instance, single and multi-unit recordings from the primary auditory cortex (A1) across various species (4, 15–18) have revealed that evoked neural responses to auditory stimuli are comparable across the SWC, despite the aforementioned significant changes in cortical dynamics. It is only in higher-order cortical areas downstream from A1 where evoked neural responses are notably increased during wakefulness compared to NREM sleep (4, 18). This suggests that local changes in neuronal dynamics alone cannot fully account for the differences in response propagation in the cortex, indicating that variations in synaptic strength might also play a significant role.

Regarding changes in synaptic dynamics, the synaptic homeostasis hypothesis (SHY) (9, 10) proposes that synaptic strength in many cortical circuits decreases during sleep to counterbalance the net synaptic upscaling observed during wakefulness. The increase in synaptic strength during wakefulness yields two opposing effects. Firstly, it amplifies stimulus-evoked postsynaptic currents due to the larger projecting axons of excitatory neurons compared to the more localized axons of inhibitory neurons (19–21). Consequently, synaptic upscaling can enhance the amplitude of evoked responses in secondary sensory areas, facilitating the transmission of neural responses across the cortical hierarchy. Secondly, synaptic upscaling enhances spontaneous postsynaptic currents, which are not triggered by external stimuli. *In vitro* studies have shown that an increase in spontaneous synaptic currents, when balanced to avoid overexcitation or overinhibition, decreases the amplitude of evoked responses to external stimuli (22). Therefore, synaptic upscaling simultaneously enhances and diminishes the transmission of neural responses across different cortical areas, depending on the context. This phenomenon underscores the intricate balance of synaptic dynamics and its impact on neural response transmission and processing within the cerebral cortex.

We propose a mechanism that sets up a competition between these opposing effects on evoked neural activities: the *driving effect*, which enhances transmission by amplifying stimulus-evoked postsynaptic currents, and the *pulling effect*, which reduces transmission by increasing spontaneous postsynaptic currents. Uniform synaptic upscaling during wakefulness, without favoring the driving over the pulling effect, may not sufficiently explain the improved propagation of neural responses during wakefulness. The balance between these opposing effects is essential for understanding how re-

sponse propagation and information processing occur within the cerebral cortex across different states of consciousness.

Hierarchical models of the cortex (23, 24) distinguish between excitatory connections at the circuit level. Generally, inter-excitatory connections link different cortical areas, whereas intra-excitatory connections operate within individual cortical areas. Inter-excitatory connections typically entail a driving effect that facilitates downstream transmission of neural responses, whereas intra-excitatory connections involve modulatory synapses that control local neural activity and lead to a pulling effect.

In this paper, we introduce the *heterogeneous synaptic homeostasis hypothesis* at the circuit level, suggesting that synaptic upscaling should favor inter- over intra-excitatory connections. This approach allows the driving effect, which improves the transmission of neural responses across cortical areas, to prevail over the pulling effect caused by spontaneous postsynaptic currents. The concept of heterogeneous synaptic homeostasis provides a refined perspective on balancing the driving and pulling effects within cortical circuits, emphasizing the significance of the spatial organization of cortical networks that are state–sensitive and facilitate efficient information transmission.

To investigate this hypothesis, we employed a Wilson-Cowan model, which simulates the average firing rate of a cortical column (25). The model replicates dynamics akin to those observed during NREM sleep and wakefulness (26). It has been shown that synaptic upscaling of intra-excitatory connections in a balanced configuration—where augmentation of inhibition counters overexcitation—gradually transitions the spontaneous activity of the model from NREM-like to wakefulness-like dynamics (27). In this study, we examine how adjusting the synaptic upscaling of both intra- and inter-excitatory connections (by factors β_{intra} and β_{inter}, respectively) influences evoked neural responses. Specifically, we study the responses of a single cortical column to stimuli with increasing intensity delivered via inter-excitatory connections. Finally, we explore a scenario where two cortical columns are symmetrically coupled by inter-excitatory connections. One column is perturbed while the other receives stimuli indirectly via inter-excitatory connections from the perturbed to the unperturbed column. We then analyze the effect of varying intra- and inter-synaptic upscaling on the propagation of neural responses between these columns.

Additionally, we establish a framework for quantifying stimulus-relevant information within evoked neural responses and investigate how intra- and inter-synaptic upscaling influence the amount of information that cortical populations convey about a stimulus and its propagation.

Results

We used a population rate model to simulate the activity of a single cortical column and its interaction with another symmetrically coupled column. By adjusting the strength of excitatory synaptic coupling, we transitioned the model between NREM sleep and wakefulness states. Our analysis concentrated on the effects of synaptic upscaling during these states, particularly focusing on response amplitudes to transient stimuli and the encoding of stimulus intensity in firing responses.

One-cortical-column model. A single cortical column is represented by a model comprising mutually coupled excitatory and inhibitory populations, each receiving independent Gaussian noise inputs (Fig. 1a).

Electrophysiological patterns. The model parameters (Tables 1 and 2) were configured to mimic spontaneous firing rates resembling NREM sleep. The parameter for intra-synaptic upscaling was set to 1 ($\beta_{\text{intra}} = 1$; Fig. 1b), reproducing neural dynamics akin to NREM sleep. These features include high-amplitude fluctuations (Fig. 1c(i)), a bimodal distribution (Fig. 1c(ii)), and high power in low-frequency bands (Fig. 1c(iii)) of the firing rate signals. These features remain robust even when the standard deviation of the noise in the model varies by up to 10% (Extended Data Fig. 1).

By increasing the strength of intra-synaptic excitatory connections ($\beta_{\text{intra}} > 1$; Fig. 1b), in line with SHY (9, 10), and adjusting inhibitory strengths to prevent overexcitation (Methods and Table 3), our model gradually transitions from NREM sleep dynamics to wakefulness (Extended Data Fig. 2). Firing rate signals become low amplitude (Fig. 1d(i)), show a unimodal distribution (Fig. 1d(ii)), and exhibit a relative increase in power at high-frequency bands (Fig. 1d(iii)). Additionally, the model shows a decrease in slow oscillation power (SO, 0.5-1 Hz), a key feature of NREM sleep, with increased intra-synaptic upscaling (Fig. 1e). These results demonstrate that the model effectively replicates well-established electrophysiological patterns observed during NREM sleep and wakefulness (6, 7, 28–31).

Evoked responses to stimuli. To analyze evoked responses, we applied transient stimuli to the cortical column through inter-excitatory connections (Fig. 2a). These stimuli represent presynaptic firing from an unmodeled upstream pyramidal population and vary in frequency from 10 Hz to 90 Hz in 20 Hz steps (Methods). With synaptic upscaling affecting both intra- (β_{intra}) and inter- (β_{inter}) synaptic connections, we analyzed various β_{intra} and β_{inter} combinations (Fig. 2b) to observe changes in evoked responses.

In the absence of noise, distinct evoked responses are observed during NREM sleep and wakefulness, consistent with prior experimental observations (16). During NREM sleep, where synaptic upscaling is absent ($\beta_{\text{intra}} = \beta_{\text{inter}} = 1$), responses exhibit a wave pattern characterized by an initial surge in firing rate followed by a subsequent decrease below the prestimulus equilibrium, maintaining a steady state well after stimulus offset (Fig. 2c(i)). In contrast, during wakefulness, synaptic upscaling ($\beta_{\text{intra}},\ \beta_{\text{inter}} > 1$) substantially reduces the suppression of neuronal firing following activation (Fig. 2c(ii)).

For all combinations of β_{intra} and β_{inter}, we quantified response amplitudes at stimulus offset. As seen in Fig. 2d, response amplitudes increase with stimulus intensity during both NREM sleep ($\beta_{\text{intra}} = \beta_{\text{inter}} = 1$) and wakefulness

DRAFT

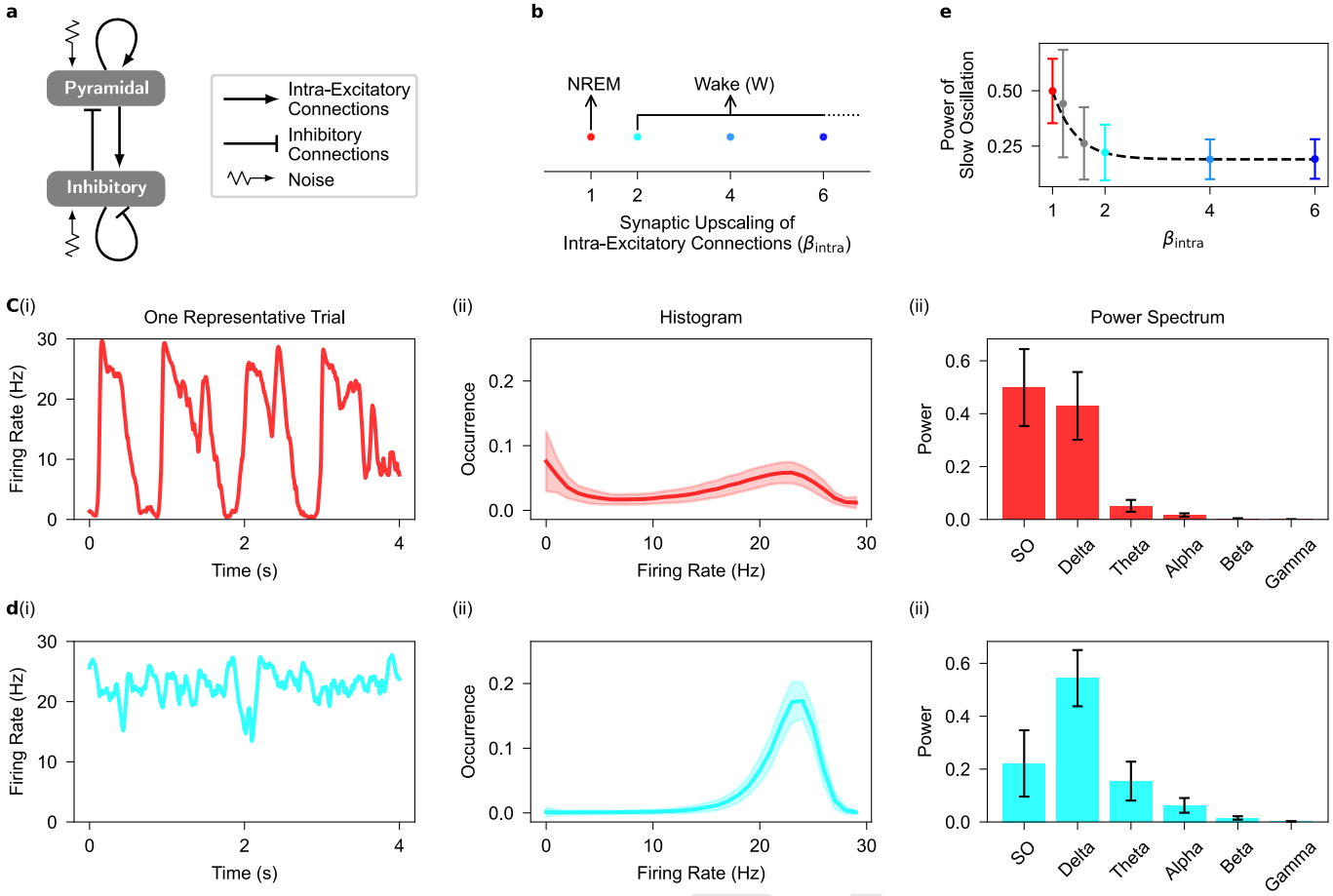

Fig. 1. Dynamical features of spontaneous firing activity in the one-cortical-column model. a, Diagram of the one-cortical-column model containing one pyramidal and one inhibitory population, where each population receives independent noise. The couplings between pyramidal and inhibitory populations are intra-excitatory and inhibitory connections mediated through, respectively, intra-AMPAergic and GABAergic synapses (Methods). Refer Table 1,2 for parameter description and values, respectively. **b**, Parameter space for synaptic upscaling of intra-excitatory connections (β_{intra}). **c**, Spontaneous firing rate signal for a representative trial (i), the distribution of firing rate signals (ii), and the power spectrum of signals (iii) when there is no intra-synaptic upscaling ($\beta_{\text{intra}} = 1$). The model produces electrophysiological features of NREM sleep when $\beta_{\text{intra}} = 1$. **d**, As in **c**, but for when intra-excitatory connections are upscaled ($\beta_{\text{intra}} = 2$). The model produces electrophysiological features of wakefulness when intra-excitatory connections are upscaled ($\beta_{\text{intra}} > 1$). **e**, The power ratio of slow oscillation (SO) gradually decreases with increasing intra-synaptic upscaling, color coded as in **b**. Shaded area and Error bar correspond to standard deviation over 500 trials. SO, <1 Hz; Delta, 1-4 Hz; Theta, 4-7 Hz; Alpha, 7-13 Hz; Beta, 3-30 Hz; Gamma, 30-100 Hz.

(β_{intra}, $\beta_{\text{inter}} > 1$), with NREM sleep generally producing larger amplitudes (red dots in Fig. 2d). Moreover, during wakefulness, keeping β_{inter} constant and increasing β_{intra} decreases evoked response amplitudes due to the aforementioned pulling effect (e.g., $\beta_{\text{inter}} = 2$ and β_{intra} from 2 to 6, shown by light to dark blue dots in Fig. 2d(i)). This pattern holds true across various β_{inter} values (e.g., $\beta_{\text{inter}} = 3$ and β_{intra} from 2 to 6, shown by light to dark green dots in Fig. 2e). This pulling effect for intra-synaptic upscaling aligns with the reduced amplitude of evoked responses observed in *in vitro* studies as spontaneous postsynaptic currents increase (22).

Conversely, keeping β_{intra} constant and increasing β_{inter} increases evoked response amplitudes due to the driving effect (e.g., $\beta_{\text{intra}} = 2$ and β_{inter} from 2 to 6, shown by the lightest blue, green, and yellow dots in Fig. 2d(ii)). Notably, in the single cortical column architecture, increasing β_{inter} exclusively modulates synapses conveying external stimuli, thus not affecting spontaneous postsynaptic currents and preventing a pulling effect.

While both intra- and inter-synaptic upscalings enhance excitatory synaptic currents upon stimulation, the net evoked synaptic current, quantified as $|\text{E}| - |\text{I}|$, decreases with increasing β_{intra} and increases with increasing β_{inter} (Extended Data Fig. 3a). This highlights the distinct effects of intra- and inter-synaptic upscaling on the evoked synaptic currents during the sleep-waking transition (Extended Data Fig. 3b). Modulating β_{intra} and β_{inter} independently allows us to define three distinct synaptic upscaling configurations characterizing the NREM-to-wakefulness transition (Fig. 2b). These are distinguished by the synaptic upscaling ratio, $\beta_{\text{inter}}/\beta_{\text{intra}}$, as follows:

1. Local-selective upscaling (LS): characterized by $\beta_{\text{inter}}/\beta_{\text{intra}} < 1$.

2. Homogeneous upscaling (H): characterized by $\beta_{\text{inter}}/\beta_{\text{intra}} = 1$.

3. Distance-selective upscaling (DS): characterized by $\beta_{\text{inter}}/\beta_{\text{intra}} > 1$.

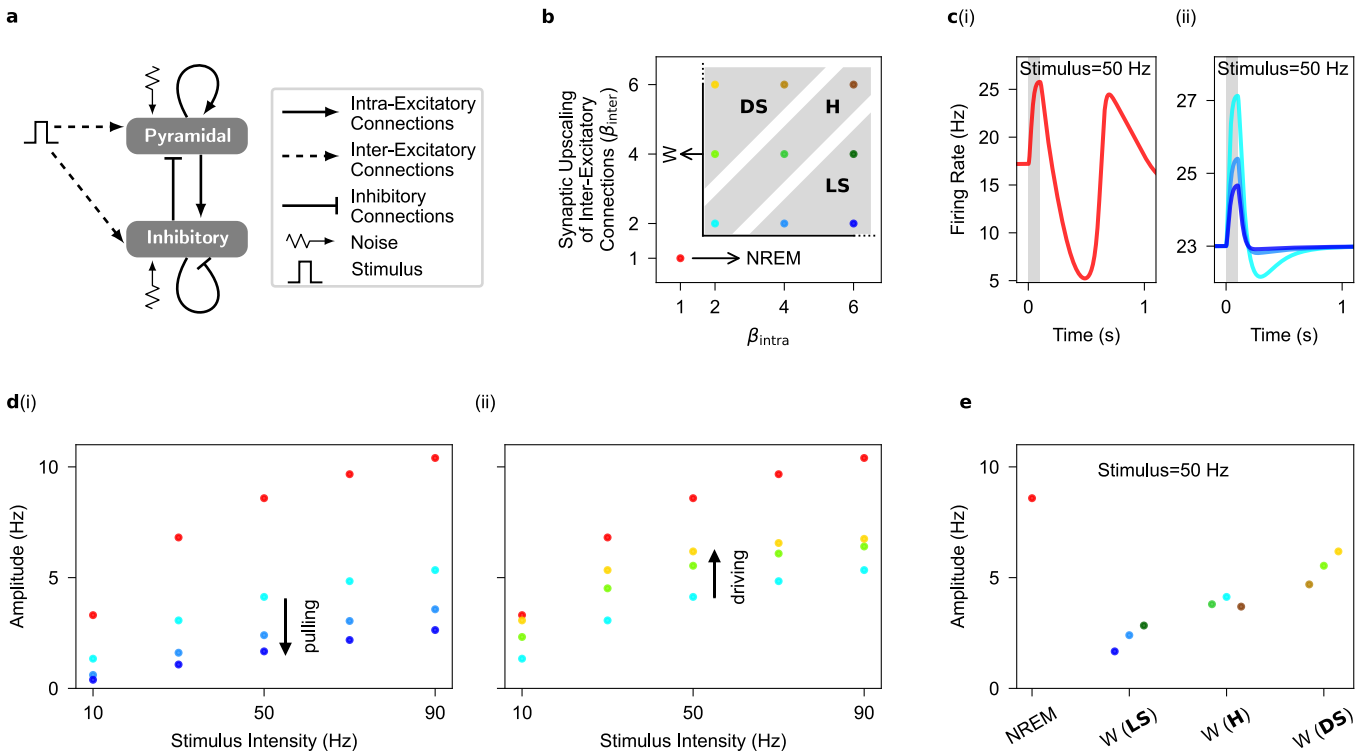

Fig. 2. Evoked firing responses to stimuli in the one-cortical-column model. a, as in Fig. 1**a**, but for when the model is subjected to stimuli. Stimuli are applied through inter-excitatory connections mediated through inter-AMPAergic synapses. Note that the noise term is set to zero for noise-free evoked response. **b**, as in Fig. 1**a**, but for when intra- and inter-excitatory connections are upscaled in wakefulness. Note that synaptic upscaling in wakefulness can occur under three synaptic upscaling configurations: Local-Selective (LS: $\beta_{\text{intra}} > \beta_{\text{inter}} > 1$), Homogeneous (H: $\beta_{\text{intra}} = \beta_{\text{inter}} > 1$), and Distance-Selective (DS: $\beta_{\text{inter}} > \beta_{\text{intra}} > 1$). **c**, The evoked firing response in NREM sleep (i) and wakefulness (ii), color coded as in Fig. 2**b**, when the stimulus intensity is 50 Hz (the evoked firing responses for other synaptic upscalings in wakefulness are not shown here). Shaded area corresponds to the stimulus duration. **d**, Increasing intra-synaptic upscaling (from $\beta_{\text{intra}} = 2$ to $\beta_{\text{intra}} = 6$) while inter-synaptic upscaling is constant ($\beta_{\text{inter}} = 2$) during wakefulness produces a pulling effect on the amplitude of evoked firing responses (i). On the other hand, increasing inter-synaptic upscaling (from $\beta_{\text{inter}} = 2$ to $\beta_{\text{inter}} = 6$) while intra-synaptic upscaling is constant ($\beta_{\text{intra}} = 2$) during wakefulness produces a driving effect on the amplitude of evoked firing responses (ii). **e**, The amplitude of evoked firing responses increases with increasing values of synaptic upscaling ratio, $\beta_{\text{inter}}/\beta_{\text{intra}}$, during wakefulness. Data points during wakefulness are organized based on increasing values of synaptic upscaling ratio on the x-axis from darkest blue to the lightest yellow. Note that in the homogeneous case, the value of $\beta_{\text{inter}}/\beta_{\text{intra}}$ is equal to one for all three data points. The amplitude of evoked firing responses increases as the synaptic upscaling transitions from local-selective (LS) to distance-selective (DS) upscaling during wakefulness.

Presenting findings based on $\beta_{\text{inter}}/\beta_{\text{intra}}$ provides a clearer representation than individual parameters. Firing rate response amplitudes during wakefulness increase with higher synaptic upscaling ratios (Fig. 2e and Extended Data Fig. 4), reaching maximum values for the DS policy.

Information about stimulus intensity. We quantify stimulus-related information in population firing rates by comparing information detection and differentiation (Methods). Information detection quantifies the performance of an optimal classifier in distinguishing evoked responses from spontaneous firing activities. Information differentiation quantifies the performance of an optimal classifier in distinguishing evoked responses elicited by different stimulus intensities from one another.

Information detection increases with stimulus intensity during both NREM sleep and wakefulness (Fig. 3a). However, increasing β_{intra} in the LS policy decreases information detection (light and dark blue dots in Fig. 3a), revealing the pulling effect. Conversely, the driving effect observed with increasing β_{inter} in the DS policy during wakefulness enhances information detection beyond NREM levels (light blue and light yellow dots in Fig. 3a; Fig. 3b and Extended Data Fig. 5).

Importantly, the higher trial-averaged amplitudes of evoked responses during NREM sleep compared to wakefulness need to be examined with increased variability across trials. Indeed, the distribution of evoked responses and spontaneous firing activities remain less distinguishable during NREM sleep than wakefulness, compromising information detection in NREM sleep.

Information differentiation during wakefulness exceeds NREM sleep levels under the DS policy (Fig. 3c). It decreases with increased intra-synaptic upscaling (light and dark blue dots in Fig. 3c), but improves with inter-synaptic upscaling (light blue and light yellow dots in Fig. 3c). This shows consistent encoding of stimulus intensity in firing rates during wakefulness compared to NREM sleep, underscoring the significance of heterogeneous synaptic upscaling favoring inter- over intra-synaptic connections.

Two-cortical-column model. In this section, we investigate the dynamics of an extended model consisting of two identical cortical columns symmetrically coupled by inter-excitatory connections (Fig. 4a).

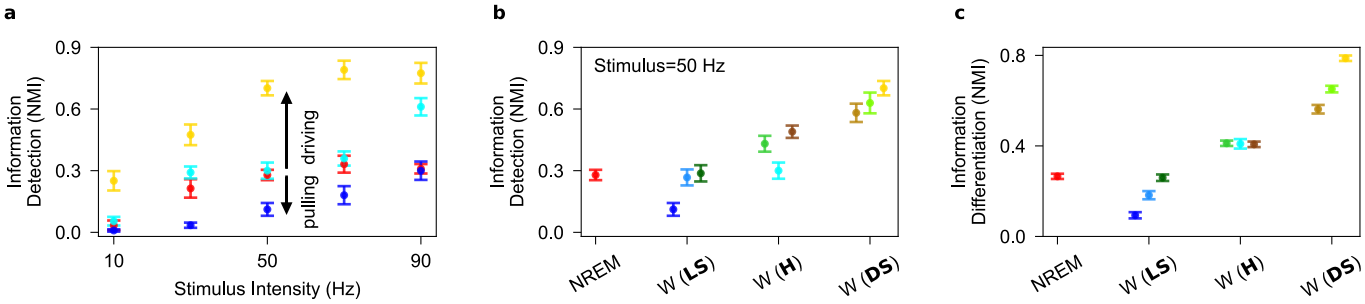

Fig. 3. Information content in the evoked firing responses to stimuli in the one-cortical-column model. **a**, Increasing intra-synaptic upscaling while inter-synaptic upscaling is constant (from $\beta_{\text{intra}} = 2, \beta_{\text{inter}} = 2$ to $\beta_{\text{intra}} = 6, \beta_{\text{inter}} = 2$) during wakefulness produces a pulling effect on information detection. On the other hand, increasing inter-synaptic upscaling while intra-synaptic upscaling is constant (from $\beta_{\text{intra}} = 2, \beta_{\text{inter}} = 2$ to $\beta_{\text{intra}} = 2, \beta_{\text{inter}} = 6$) during wakefulness produces a driving effect on information detection. **b**, Information detection increases as the synaptic upscaling transitions from local-selective (LS) to distance-selective (DS) upscaling during wakefulness compared to NREM sleep. Note that data during wakefulness is organized based on increasing values of $\beta_{\text{inter}}/\beta_{\text{intra}}$ on the x-axis. **c**, As in **b**, but for information differentiation. Information differentiation increases as the synaptic upscaling transitions from local-selective (LS) to distance-selective (DS) upscaling during wakefulness compared to NREM sleep. Error bar corresponds to 95% confidence interval over 10 performance estimate of the K-means clustering algorithms.

Electrophysiological patterns. The analysis of spontaneous firing activities in the two-cortical-column model replicates the findings of the single-cortical-column model. Increasing β_{intra} and β_{inter} to mimic synaptic upscaling from sleep to wakefulness reduces the amplitude of spontaneous fluctuations in pyramidal neuron firing rates (Extended Data Fig. 6). Notably, the power of the SO band during NREM sleep decreases compared to the single cortical column scenario (Extended Data Fig. 6a and Fig. 1c), supporting experimental findings that cortical de-afferentiation enhances NREM-like dynamics (13).

Evoked responses to stimuli. The two-cortical-column architecture serves as a model for exploring downstream information processing from a primary to a secondary cortical sensory area. One column, termed the *perturbed* cortical column, directly receives a stimulus, akin to a primary sensory area receiving direct unimodal thalamic signals. The stimuli modeled in the one-cortical-column model are used here as well. The other column, termed the *unperturbed* cortical column, detects the stimulus solely through presynaptic connections from the perturbed cortical column, mirroring higher-order unimodal sensory areas.

In the absence of noise, the evoked responses of both perturbed and unperturbed populations at stimulus offset reproduce those observed in the single-column model (Extended Data Fig. 7 and Fig. 2d,e). Increasing β_{intra} in the LS policy reduces response amplitudes in both populations (light to dark blue dots in Extended Data Fig. 7a), while increasing β_{inter} in the DS policy enhances them (light blue to light yellow dots in Extended Data Fig. 7a). Transitioning from LS to DS upscaling, by increasing the $\beta_{\text{inter}}/\beta_{\text{intra}}$ ratio, boosts response amplitude to external stimuli in both populations (Extended Data Fig. 7b).

In the two-cortical-column model, both intra- and inter-synaptic upscaling boost spontaneous synaptic activity in the unperturbed population, indicating a *pulling* effect now exerted by inter-excitatory connections. Nonetheless, inter-synaptic upscaling generates an overall driving effect as the net evoked synaptic current increases with increasing inter-synaptic upscaling, contrasting with intra-synaptic upscaling (Extended Data Fig. 7c).

Information about stimulus intensity. Encoding of stimulus intensity in the firing rate of the perturbed population increases from LS to DS upscaling (Fig. 4b and Extended Data Fig. 8a). DS upscaling is the only policy that increases information beyond NREM sleep levels. In the unperturbed population, both information detection and differentiation greatly surpass NREM sleep levels during DS upscaling (Fig. 4c and Extended Data Fig. 8b).

These results highlight the necessity for synaptic upscaling across the SWC to be spatially heterogeneous. Specifically, synapses between distinct cortical areas (inter-synapses) must be upscaled more than recurrent synapses within cortical areas (intra-synapses) throughout the SWC. This heterogeneity ensures better stimulus-encoded information during wakefulness compared to NREM sleep across the sensory processing chain.

Robustness of the Computational Results. To quantify information content, we employed unsupervised machine learning techniques, such as K-means clustering algorithms. Our results remain consistent applying supervised machine learning techniques, such as logistic classification algorithms (Extended Data Fig. 9a).

Furthermore, our findings are robust across different analytical approaches. Significance tests qualitatively reproduce findings on information detection and differentiation (Methods and Extended Data Fig. 9b). Moreover, using information theory to compute the mutual information (MI) between the distribution of evoked responses at the stimulus offset and the distribution of stimuli reveals that MI increases as synaptic upscaling transitions from LS to DS upscaling policy (Extended Data Fig. 9c).

Discussion

Substantial differences exist in the discharge pattern of the AAN in the brainstem across various states of consciousness (32, 33), resulting in alterations in neuromodulator concentrations throughout the brain (5). These molecular

DRAFT

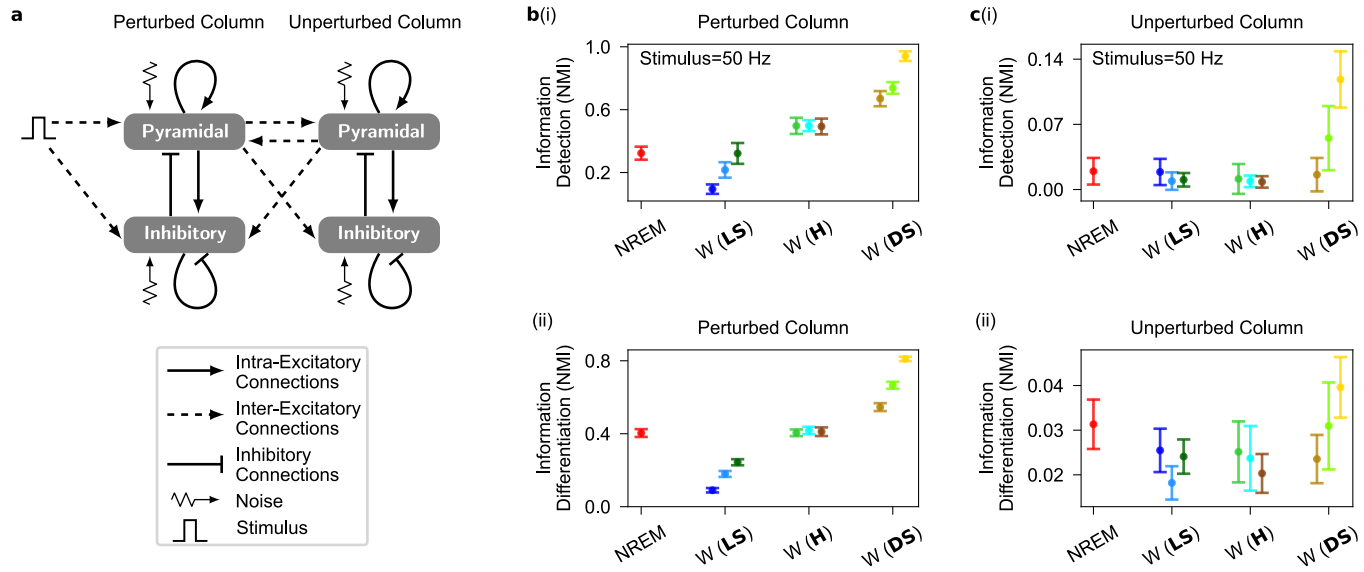

Fig. 4. Evoked firing responses to stimuli in the two-cortical-column model. a, Diagram of the two-cortical-column model, where each population receives independent noise. The couplings between the two columns are symmetric and are inter-excitatory connections mediated through inter-AMPAergic synapses (Tables 1, 4, 5 for symbol description and parameter values). In the context of spontaneous firing activity, stimulus inensity is set to zero. Note that the noise term is set to zero for noise-free evoked response. **b**, Information detection (i) and differentiation (ii) in the perturbed cortical column increase with increasing values of β_{intra} and β_{inter} and as the synaptic upscaling transitions from local-selective to distance-selective upscaling during wakefulness compared to NREM sleep. **c**, As in **b**, but for the unperturbed cortical column. Information detection (i) and differentiation (ii) in the unperturbed cortical column increase as the synaptic upscaling transitions from local-selective to distance-selective upscaling during wakefulness compared to NREM sleep. Error bar corresponds to 95% confidence interval over 10 performance estimate of the K-means clustering algorithms.

changes impact neuronal (6, 7) and synaptic (8–10) dynamics, potentially altering the cortex's ability to efficiently transmit neural signals (1–4). Nevertheless, the direct causal relationships between these biological layers remain unclear.

This research investigates the relationship between the synaptic upscaling of excitatory connections (8–10) and enhanced cortical effective connectivity (2–4) during the transition from NREM sleep to wakefulness. Through computational modeling, we offer insights into how synaptic upscaling of excitatory connections not only induces dynamic changes in the electrical activity of the neural networks but also alters information propagation across these networks. Our results show that a spatially broader propagation of information and neural responses occurs during wakefulness compared to NREM sleep, provided that synaptic upscaling between distinct networks surpasses that of local and recurrent connections.

Our result aligns with several previously published computational studies. Firstly, the strengthening of inter-areal excitatory connections in a balanced configuration has been shown to enhance signal transmission in a network model of the macaque cortex (34). Secondly, this outcome aligns with findings that rare long-range connections are necessary for information processing (35).

Our study concentrates on the interaction between two cortical columns, excluding whole-brain interactions. A more detailed model including various cortical and subcortical structures might offer additional insights into the spatial distribution of synaptic scaling. In our simplified model, the connections between the two cortical columns are excitatory and symmetrical, potentially not capturing the full complexity of structural connectivity across all cortical regions. Future work could benefit from distinguishing between feedforward and feedback excitatory connections to better understand how distinct modulations of synaptic upscaling affect propagation of information and neural response. Nonetheless, these would not invalidate the core concept of the DS synaptic upscaling policy as our conclusions hold true even when limited to a single cortical column, showing that DS synaptic upscaling improves stimulus-induced information encoding. Moreover, our neural mass model presupposes that neural communication is based on rate coding. Future investigations could explore spiking-based models since our hypothesis is not conditioned by the coding scheme (temporal or rate based).

A significant contribution of our study is the development of a framework for measuring informational content within neural signals. Most studies in sleep research have not explicitly evaluated information content and are primarily based on the amplitude of evoked neural signals. Our work addresses this gap by showing that neither information encoding nor its propagation are enhanced in wakefulness over NREM sleep, except when inter-synaptic upscalings surpass intra-synaptic upscalings. The robustness of our findings is supported by employing a variety of analytical methods, including unsupervised and supervised machine learning techniques, alongside statistical tests and information theory.

Recent studies highlight the significance of analyzing informational content. Research using Neuropixels probes in mice shows that burst firing in thalamic neurons and amplitude of cortical responses to electrical stimulation are highest during quiet wakefulness and lowest during anesthesia (36). Since thalamic neurons tend to fire in bursts during NREM sleep (37–39), we might expect similar high activity lev-

DRAFT

els in thalamic relay neurons during NREM sleep as during quiet wakefulness, despite reduced cortical response amplitudes. Our research suggests that distinguishing between information detection and differentiation in stimulus-evoked activity could explain how cortico-thalamo-cortical connections adjust information transfer during quiet wakefulness and NREM sleep.

Wakefulness is associated with consciousness and the capacity to respond to environmental stimuli, whereas sleep diminishes sensory perception (40–42). Human EEG studies show the sleeping brain can perform basic auditory tasks, although higher cognitive functions are compromised. For instance, cognitive response to the subjects' own name during sleep is similar to that observed during wakefulness (43), whereas motor preparation in response to auditory stimuli are attenuated during NREM sleep relative to wakefulness (41). Moreover, sensory encoding of intelligible stories attenuates during NREM sleep compared to wakefulness, despite comparable encoding of unintelligible stories (42). These results point toward the diminished capacity of the brain to process sensory information with a higher cognitive demand during NREM sleep. Our findings suggest that heterogeneous synaptic upscaling from sleep to wakefulness enhances information detection and differentiation across a broader region of the cortex, allowing for more complex cognitive computations.

Our findings suggest reevaluating the SHY with a focus on circuit-level heterogeneity. Although our results need further empirical support, evidence exists for cellular-level heterogeneity in synaptic upscaling, particularly between perforated and non-perforated synapses. Perforated synapses are larger with discontinuous post-synaptic densities (PSDs), while non-perforated ones are smaller with continuous PSDs (44). Perforated synapses in the mouse cerebral cortex expand their axon-spine contact area upon waking, unlike non-perforated synapses (44). This structural difference highlights a selective approach to synaptic homeostasis at the cellular level. Further experiments are required to explore if cellular-level synaptic homeostasis heterogeneity aligns with our circuit-level hypothesis.

Heterogeneous synaptic upscaling increases the recruitment of a wider network of neural populations across the cortical hierarchy during wakefulness compared to sleep, which is necessary for the emergence of various collective computations within networks of interconnected neurons (45). Yet, the mechanism behind heterogeneous synaptic homeostasis remains unclear. We offer a speculative explanation: intra-synaptic and inter-synaptic connections lie on different dendritic segments, each with a distinct receptor density for neuromodulators secreted by the AAN. Thus, the heterogeneity in receptor expressions results in the heterogeneous synaptic homeostasis during the SWC.

In a wider perspective, heterogeneity seems to be the norm rather than the exception within the brain. For instance, neural firing in pyramidal cells differs based on their target destinations, indicating heterogeneity within traditional pyramidal cell types (46). Moreover, the developmental and regional distribution of N-methyl-D-aspartate (NMDA) receptors have been observed to be heterogeneous (47).

Research indicates that neural heterogeneity plays a functional role in the brain. It improves information transfer in spiking neural networks (48), enhances coding efficiency in predictive coding models (49), acts as a homeostatic mechanism preventing seizures (50), and supports stable learning in recurrent neural networks (51). Our findings contribute to this field by showing that the increased cortical effective connectivity observed during wakefulness relative to NREM sleep may arise from heterogeneous synaptic homeostasis.

Methods

The computational model used in this study has been implemented in previous studies (25–27). Briefly, we employed a neural mass model (25) to replicate the average firing rate of a neural cortical column. The model captures the fundamental characteristics of both NREM sleep and wakefulness (26, 27).

One-Cortical-Column Model. A single cortical column is composed of interconnected pyramidal (p) and inhibitory (i) populations (Fig. 1a).

Neural Mass Model. The average firing rate of each population is represented as an instantaneous function of the average membrane potential, denoted as $V_{p/i}$, using a sigmoid function (25, 52):

$$Q_k(V_k) = Q_k^{max} \frac{(1+\tanh(C(V_k-\theta_k)/\sigma_k))}{2}, \quad \textbf{(1)}$$

where $k \in \{p, i\}$. Q_k^{max}, θ_k, and σ_k correspond to, respectively, the maximum firing rate, firing rate threshold, and inverse neural gain of population p or i (Table 1,2 for symbol descriptions and parameter values). The constant C equals to $\frac{\pi}{2\sqrt{3}}$ and establishes the connection between the neural gain and the slope of the sigmoid function (26). This nonlinear function aligns with experimental observations indicating that the firing rate and membrane potential of cortical neurons *in vivo* follow a non-linear increasing pattern (7).

Model Synapses. Connections between populations are modeled by dynamic synapses. Synapses within the model are characterized by presynaptic and postsynaptic elements. The presynaptic element consists of intrinsic and extrinsic activities. Intrinsic activity arises from explicitly modeled pyramidal and inhibitory populations, while extrinsic activity originates from nearby, non-explicitly modeled cortical columns. The extrinsic activity affects populations p and i exclusively through excitatory synapses. This is consistent with the morphology of cortical neurons, in which pyramidal neurons have larger projecting axons than the more localized inhibitory axons (19–21). This has also been reflected in numerous computational studies (53–57).

Our model follows Dale's principle, which dictates that excitatory populations exert excitatory effects on all synaptic connections, while inhibitory populations exert inhibitory

DRAFT

Table 1. Parameter description in the one-cortical-column model.

Symbol	Description
$Q_k^{\max}$	Maximal firing rate of population k
θ_k	Firing rate threshold of population k (sigmoid function half activation)
σ_k	Inverse neural gain of the sigmoid function of population k
τ_k	Membrane time constant of population k
C_m	Membrane capacitance in the HH model
ϕ_k	Gaussian noise on population k
$N_{kk'}$	Mean number of synaptic connections from population k' to population k
γ_m	Time constant of the postsynaptic response of synapse type m
$\bar{g}_{\mathrm{X}}$	Average X-ergic conductance
E_{X}	Reversal potential of the X-ergic current
$\bar{g}_{\mathrm{KNa}}$	Average conductance of sodium-dependent potassium channel
E_{K}	Nernst reversal potential of potassium channel
τ_{Na}	Time constant of sodium extrusion
α_{Na}	sodium influx through population firing rate
R_{pump}	Strength of the sodium pump
$\mathrm{Na}_{\mathrm{eq}}$	Resting state sodium concentration equilibrium
β_{intra}	Synaptic-upscaling factor for intra-excitatory connections
β^k_{GABA}	Synaptic-upscaling factor for inhibitory connections on population k

Table 2. Parameter values in the one-cortical-column model.

Symbol	Value	Unit
$Q_p^{\max}$	30	Hz
$Q_i^{\max}$	60	Hz
θ_p, θ_i	-58.5	mV
σ_p	6.7	mV
σ_i	6	mV
τ_p, τ_i	30	ms
C_m	1	$\mu\mathrm{F/cm}^2$
$\phi_{p/i}$	1.2	ms^{-1}
N_{pp}	144	–
N_{ip}	36	–
N_{pi}	160	–
N_{ii}	40	–
γ_p	$70 \cdot 10^{-3}$	ms^{-1}
γ_i	$58.6 \cdot 10^{-3}$	ms^{-1}
$\bar{g}_{\mathrm{AMPA}}$	1	ms
$\bar{g}_{\mathrm{GABA}}$	1	ms
E_{AMPA}	0	mV
E_{GABA}	-70	mV
E_{L}^p	-66	mV
E_{L}^i	-64	mV
$\bar{g}_{\mathrm{KNa}}$	1.9	$\mathrm{mS/cm}^2$
E_{K}	-100	mV
τ_{Na}	1.7	ms
α_{Na}	2	$\mathrm{mM} \cdot \mathrm{ms}$
R_{pump}	0.09	mM
$\mathrm{Na}_{\mathrm{eq}}$	9.5	mM
β_{intra}	1	–
$\beta^{p/i}_{\mathrm{GABA}}$	1	–

effects, regardless of the identity of the target population. The postsynaptic component is characterized by ionotropic receptors, which include α-amino-3-hydroxy-5-methyl-4-isoxazolepropionic acid (AMPA) and γ-aminobutyric acid (GABA) receptors. To clarify, we consider synapses to be AMPAergic when they produce excitatory effects, which occurs when the presynaptic population is excitatory. Conversely, we categorize synapses as GABAergic when they generate inhibitory effects, and this happens when the presynaptic population is inhibitory. Henceforth, we will use the term *intra-excitatory connections* to refer to excitatory connections within a cortical column, which are mediated through intra-AMPAergic synapses.

The mathematical framework utilized to describe synapses involves convolving the presynaptic firing rate, $Q_{k'}$, with the average synaptic response to a single spike, $\alpha_{k'}$, which exhibits an exponential decay time course (58):

$$s_{kk'} = N_{kk'} Q_{k'}(V_{k'}) \circledast \alpha_{k'}, \quad \textbf{(2)}$$

$$\alpha_{k'} = \gamma_{k'}^2 \, t \, \exp(-\gamma_{k'} t), \quad \textbf{(3)}$$

where $N_{kk'}$ represents the average number of synaptic connections from the presynaptic population k' to the postsynaptic population k. The parameter $\gamma_{k'}$ characterizes the time constant governing the dynamics of a synapse activated by the presynaptic firing of population k'. The combination of equations (2) and (3) leads to a second-order differential equation:

$$\ddot{s}_{kk'} = \gamma_{k'}^2 \left(N_{kk'} \, Q_{k'}(V_{k'}) + \phi_k - s_{kk'} \right) - 2\gamma_{k'} \, \dot{s}_{kk'}, \quad \textbf{(4)}$$

Equation (4) describes the synaptic current dynamics resulting from the firing of the presynaptic population k' on the postsynaptic population k. Additionally, noise, denoted as

DRAFT

ϕ_k, is independently simulated for each cortical population as a Gaussian process with zero autocorrelation time, zero mean, and a standard deviation of 1.2 ms^{-1}. Notably, the application of Gaussian noise is limited to intra-excitatory connections. The intra-AMPAergic and GABAergic synaptic currents are defined as follows:

$$I^k_{intra\text{-AMPA}} = \beta_{\text{intra}}\, \bar{g}_{\text{AMPA}}\, s_{kp}\, (V_k - E_{\text{AMPA}}), \quad \textbf{(5)}$$

$$I^k_{\text{GABA}} = \beta^k_{\text{GABA}}\, \bar{g}_{\text{GABA}}\, s_{ki}\, (V_k - E_{\text{GABA}}), \quad \textbf{(6)}$$

here, β_{intra} and β^k_{GABA} are scaling factors for intra-excitatory connections and inhibitory connections on population k, respectively. $\bar{g}_{\text{AMPA}}$ and $\bar{g}_{\text{GABA}}$ correspond to the average AMPAergic and GABAergic conductances, while E_{AMPA} and E_{GABA} represent the reversal potentials for AMPAergic and GABAergic currents, respectively.

The dynamics of the average membrane potential for each cortical population ($V_{p/i}$) are determined using the mathematical formalism of the classical conductance-based model (59). This model encompasses one leak, two synaptic currents, and an activity-dependent potassium current, as described by the following equations:

$$\tau_p \dot{V}_p = -I^p_{\text{L}} - I^p_{intra\text{-AMPA}} - I^p_{\text{GABA}} - \tau_p C_m^{-1} I_{\text{KNa}}, \quad \textbf{(7)}$$

$$\tau_i \dot{V}_i = -I^i_{\text{L}} - I^i_{intra\text{-AMPA}} - I^i_{\text{GABA}}, \quad \textbf{(8)}$$

Here, $\tau_{p/i}$, $I^{p/i}_{\text{L}}$, $I^{p/i}_{intra\text{-AMPA}}$, and $I^{p/i}_{\text{GABA}}$ represent, respectively, the membrane time constant, leak, intra-AMPAergic, and GABAergic currents of population p or i. The variable I_{KNa} denotes the activity-dependent potassium current specific to the pyramidal population, which is detailed in the following subsection. Additionally, C_m signifies the membrane capacitance in the Hodgkin–Huxley model.

Activity-Dependent Potassium Current. The slow oscillation is a prominent feature of neuronal cortical activity during NREM sleep, characterized by alternating active (Up) and silent (Down) firing patterns. The initiation of the Down state has been hypothesized to involve the activation of the slow activity-dependent K^+ current, as suggested in previous studies (28, 29, 31). The sodium-dependent potassium current I_{KNa} and sodium concentration [Na] are incorporated into the model as follows:

$$I_{\text{KNa}} = \bar{g}_{\text{KNa}}\, \frac{0.37}{1 + (\frac{38.7}{[\text{Na}]})^{3.5}}\, (V_p - E_{\text{K}}), \quad \textbf{(9)}$$

$$\tau_{\text{Na}}\, [\dot{\text{Na}}] = \alpha_{\text{Na}} Q_p(V_p) - \text{Na}_{\text{pump}}([\text{Na}]), \quad \textbf{(10)}$$

In these equations, $\bar{g}_{\text{KNa}}$, E_{K}, τ_{Na}, and α_{Na} represent the average conductance of I_{KNa}, the Nernst reversal potential of the I_{KNa} current, the time constant governing the extrusion of sodium concentration, and the average influx of sodium concentration per firing event, respectively. The function Na_{pump} accounts for sodium pumps that regulate the removal of sodium ions.

Synaptic Upscaling of Intra-Excitatory Connections. The average conductance of intra-excitatory connections within the one-cortical-column model are upscaled by a factor of β_{intra}. Primarily, we demonstrate that the one-cortical-column model generates NREM-like dynamics when there is no synaptic upscaling, i.e., $\beta_{\text{intra}} = 1$. Next, we show that intra-synaptic upscaling induces a transition in the dynamics from NREM sleep to wakefulness, in line with the concept of synaptic homeostasis hypothesis (9, 10) and the influence of active neuromodulatory stimuli on synaptic upscaling from subcortical regions (5, 8).

In the one-cortical-column model, synaptic upscaling of intra-excitatory connections within the cortical column is achieved by increasing the parameter β_{intra}. The intra-synaptic upscaling process is carried out in a balanced configuration. To elaborate, it involves enhancing inhibition to counteract overexcitation within each population. Consequently, the average conductance of inhibitory connections is augmented in both pyramidal and inhibitory populations. This augmentation is governed by the factors β^p_{GABA} and β^i_{GABA}, respectively (Table 3 for parameter values).

Table 3. Parameter values of β^k_{GABA} for intra-synaptic upscalings in wakefulness in the one-cortical-column model.

	$\beta_{\text{intra}} = 2$	$\beta_{\text{intra}} = 3$	$\beta_{\text{intra}} = 4$
β^p_{GABA}	1.961	4.724	7.488
β^i_{GABA}	2.165	4.65	7.134

This approach ensures that the intra-synaptic upscalings remain in balance by maintaining the steady-state values of the average membrane potential for both pyramidal (V_p) and inhibitory (V_i) populations, aligning them with their respective values during the Up state in NREM sleep. This is in agreement with experimental findings that reported dynamics of neural signals in Up states during NREM sleep are similar to those of continuous wakefulness (7, 60).

The values of V_p and V_i during Up state in NREM sleep (when there is no synaptic upscaling: $\beta_{\text{intra}} = 1$) are determined through 500 simulations, each lasting 4 seconds. During NREM sleep, the distribution of firing rate signals exhibits a bimodal pattern, with the polarized peak being associated with the Up states. The peak value of the distribution of firing rate signals during Up states is employed to calculate the steady-state values of V_p and V_i in wakefulness. The parameters β^p_{GABA} and β^i_{GABA}, pertaining to pyramidal and inhibitory populations, respectively, are adjusted to align V_p and V_i with their counterparts during the Up state for a given intra-synaptic upscaling parameter, β_{intra}, in wakefulness. For the complete model equations, please refer to Appendix . Further details regarding the dynamical constraints governing β^p_{GABA} and β^i_{GABA} for pyramidal and inhibitory populations in the one-cortical-column model are available in Appendix .

Two-Cortical-Column Model. We have expanded the model to encompass two bidirectionally connected cortical columns (Fig. 4a). The parameters for each individual cor-

DRAFT

tical column remain consistent with those described in the one-cortical-column model. Our assumption is that the connectivity between these two cortical columns is both symmetrical and excitatory. This is attributed to the longer axons of pyramidal neurons compared to the shorter axons of inhibitory neurons, as substantiated by previous studies (19–21, 53–55, 57). For the sake of notation convenience, we will utilize p and i to denote the pyramidal and inhibitory populations in the first cortical column, and p' and i' to denote populations in the second cortical column (Table 4 for the specific values of connectivity between the two cortical columns).

Table 4. Parameter values of connectivity in the two-cortical-column model.

Symbol	Value	Description
$N_{pp'}$, $N_{p'p}$	16	Mean number of synaptic connections from p to p' (and p' to p)
$N_{ip'}$, $N_{i'p}$	4	Mean number of synaptic connections from p to i' (and p' to i)

In the context of the two-cortical-column model, we will refer to excitatory synapses connecting the two columns as *inter-excitatory connections*, distinguishing them from the *intra-excitatory connections* within each individual cortical column.

In accordance with the description provided, the second-order differential equations for inter-AMPAergic postsynaptic responses in the first cortical column due to the inter-excitatory connections coupling are expressed as follows:

$$\ddot{s}_{pp'} = \gamma_{p'}^2 \left(N_{pp'}\, Q_{p'}(V_{p'}) - s_{pp'}\right) - 2\gamma_{p'}\, \dot{s}_{pp'}, \quad \textbf{(11)}$$

$$\ddot{s}_{ip'} = \gamma_{p'}^2 \left(N_{ip'}\, Q_{p'}(V_{p'}) - s_{ip'}\right) - 2\gamma_{p'}\, \dot{s}_{ip'}, \quad \textbf{(12)}$$

Here, $N_{kp'}$ represents the mean number of synaptic connections from a presynaptic pyramidal population p' in the second cortical column to postsynaptic populations k, $k \in \{p,\ i\}$, in the first cortical column. Consequently, the inter-AMPAergic current to the postsynaptic population k in the first cortical column can be defined as:

$$I^k_{inter\text{-AMPA}} = \beta_{\text{inter}}\, \bar{g}_{\text{AMPA}}\, s_{kp'}\, (V_k - E_{\text{AMPA}}), \quad \textbf{(13)}$$

Consequently, the dynamics of the average membrane potential of each cortical population, $V_{p/i}$, are determined as follows:

$$\tau_p \dot{V}_p = -I^p_{\text{L}} - I^p_{intra\text{-AMPA}} - I^p_{inter\text{-AMPA}} - I^p_{\text{GABA}} - \tau_p C_m^{-1} I_{\text{KNa}}, \quad \textbf{(14)}$$

$$\tau_i \dot{V}_i = -I^i_{\text{L}} - I^i_{intra\text{-AMPA}} - I^p_{inter\text{-AMPA}} - I^i_{\text{GABA}}, \quad \textbf{(15)}$$

Swapping indexes between the first and second cortical column results in the equations for the second cortical column. see Appendix for the full model equations.

During NREM sleep, these inter-excitatory connections increase excitation in both the pyramidal and inhibitory populations within each cortical column. To counterbalance this overexcitation, the average conductance of inhibitory connections within each cortical column is upregulated by a factor denoted as β^k_{GABA}, $k \in \{p,\ i,\ p',\ i'\}$. This adjustment is achieved by first determining the steady-state values of V_p and V_i in the one-cortical-column model through a noise-free simulation (in the absent of Gaussian noise) during NREM sleep. These values are then used to compute the corresponding β^k_{GABA}, $k \in \{p,\ i,\ p',\ i'\}$, in the two-cortical-column model during NREM sleep (for further details, please refer to Appendix for the dynamical constraints on β^k_{GABA} in the two-cortical-column model). It is important to note that due to the symmetry in the connectivity paradigm, the values for the pyramidal populations in each cortical column are identical, as are the values for the inhibitory populations (Table 5 for the parameter values of β^k_{GABA} during NREM when $\beta_{\text{intra}} = 1$ and $\beta_{\text{inter}} = 1$).

During wakefulness in the two-cortical-column model, synaptic upscaling occurs in two directions: intra-excitatory connections and inter-excitatory connections. As a result, there are three synaptic upscaling configurations in wakefulness: local-selective ($\beta_{\text{intra}} > \beta_{\text{inter}} > 1$), homogeneous ($\beta_{\text{intra}} = \beta_{\text{inter}} > 1$), and distance-selective synaptic upscaling ($\beta_{\text{inter}} > \beta_{\text{intra}} > 1$). In each of these cases, synaptic upscaling introduces overexcitation within each cortical column. To counteract this overexcitation, the average conductance of inhibitory connections within each cortical column is upregulated by β^k_{GABA}, with k representing $p,\ i,\ p',\ i'$. This adjustment is made by utilizing the values of V_p and V_i in Up states from the one-cortical-column model. Subsequently, β^k_{GABA}, with k being $p,\ i,\ p',\ i'$, is upregulated until the corresponding V_p and V_i values are achieved for the intra- and inter-synaptic upscaling in wakefulness, denoted as β_{intra} and β_{inter}, respectively (for further details, please refer to Appendix for the dynamical constraints on β^k_{GABA} in the two-cortical-column model). This ensures that the steady-state values of V_p and V_i in the two-cortical-column model align with the values in wakefulness and Up states of NREM sleep in the one-cortical-column model (Table 5 for the parameter values of β^k_{GABA} during NREM sleep when $\beta_{\text{intra}} = \beta_{\text{inter}} = 1$ and during wakefulness when $\beta_{\text{intra}} > 1, \beta_{\text{inter}} > 1$).

Computational pipeline. Simulations were implemented in Python and conducted using a stochastic Heun method (61) with a step size of 0.1 ms. The code is available on GitHub (62). Each simulation (trial) was implemented independently, with initial conditions for all variables randomly selected from a uniform distribution. Trials were simulated with a duration of 4 s, after discarding the first 4 s at the beginning of the simulation to eliminate transient dynamics and stabilize the solution.

The computational pipeline consisted of two stages. In the first stage, we simulated signals for the one-cortical-column model, and in the second stage, we extended this to the two-cortical-column model. Each stage comprised two phases. The first phase focused on simulating stochastic signals in

DRAFT

Table 5. Parameter values of β^k_{GABA}, $k \in \{p,\ i,\ p',\ i'\}$, for various synaptic upscalings in the two-cortical-column model.

	$\beta_{\text{intra}} = 1$	$\beta_{\text{intra}} = 2$			$\beta_{\text{intra}} = 4$			$\beta_{\text{intra}} = 6$		
	$\beta_{\text{inter}} = 1$	$\beta_{\text{inter}} = 2$	$\beta_{\text{inter}} = 4$	$\beta_{\text{inter}} = 6$	$\beta_{\text{inter}} = 2$	$\beta_{\text{inter}} = 4$	$\beta_{\text{inter}} = 6$	$\beta_{\text{inter}} = 2$	$\beta_{\text{inter}} = 4$	$\beta_{\text{inter}} = 6$
$\beta^{p/p'}_{\text{GABA}}$	1.18	2.268	2.575	2.882	5.032	5.339	5.646	7.795	8.102	8.409
$\beta^{i/i'}_{\text{GABA}}$	1.149	2.441	2.717	2.993	4.926	5.202	5.478	7.41	7.686	7.963

the absence of external stimuli to asses the *electrophysiological patterns* (subsection and) of the spontaneous neural activities in the respective model. Initially, 500 trials were simulated separately when excitatory synapses were not upscaled (Table 2). This showed that the model was capable of producing NREM-like dynamics. Moreover, in the one-cortical-column model, 500 independent trials were simulated separately to evaluate the robustness of NREM-like dynamics as the standard deviation of the Gaussian noise was varied by 10%. This analysis demonstrated that the NREM-like dynamics remained consistent within the examined range and was independent of the standard deviation of the Gaussian noise. Finally, 500 trials were conducted separately to explore the impact of various synaptic upscalings in a balanced configuration in the respective model. These trials revealed how synaptic upscaling could shift the dynamics from NREM-like to wakefulness-like dynamics.

In the second phase we focused on simulating signals when the respective model is subjected to stimuli with increasing stimulus intensity to asses the *evoked responses to stimuli* (subsection and). Stimuli are delivered through inter-excitatory connections and represent the strength of presynaptic firing of an unmodeled pyramidal population, denoted as $Q^{\text{stimulus}}_{p^{um}}$. We consider that the unmodeled upstream cortical column forms excitatory synapses with the pyramidal and inhibitory populations in the one-cortical-column model. The mean number of synaptic connections is specified as $N_{pp^{um}}$ and $N_{ip^{um}}$ (16 and 4, respectively). The index "um" denotes the unmodeled cortical column. The inter-AMPAergic postsynaptic response in the cortical column resulting from the firing of the unmodeled upstream cortical column is described by the equation:

$$\ddot{s}^{\text{stimulus}}_{kp^{um}} = \gamma^2_{p^{um}}\ (N_{kp^{um}}\ Q^{\text{stimulus}}_{p^{um}} - s^{\text{stimulus}}_{kp^{um}}) \\ -2\gamma_{p^{um}}\ \dot{s}^{\text{stimulus}}_{kp^{um}}, \tag{16}$$

Here, k represents either the pyramidal or the inhibitory postsynaptic population in the cortical column model. Considering the influence of inter-excitatory connections from the unmodeled cortical column, the excitatory postsynaptic current to the postsynaptic population k in response to a given stimulus intensity can be expressed as follows:

$$I^{k,\ \text{stimulus}}_{inter\text{-AMPA}} = \beta_{\text{inter}}\ \bar{g}_{\text{AMPA}}\ s^{\text{stimulus}}_{kp^{um}}\ (V_k - E_{\text{AMPA}}) \tag{17}$$

for $k \in \{p, i\}$. Taking in to account these postsynaptic currents associated with the stimulus, the equations for the dynamics of the average membrane potential of each cortical population in the one-cortical-column model, as given by equation 7 and 8, can be expressed as follows:

$$\tau_p \dot{V}_p = -I^p_{\text{L}} - I^p_{intra\text{-AMPA}} - I^p_{\text{GABA}} - \tau_p C_m^{-1} I_{\text{KNa}} \\ - I^{p,\ \text{stimulus}}_{inter\text{-AMPA}}, \tag{18}$$

$$\tau_i \dot{V}_i = -I^i_{\text{L}} - I^i_{intra\text{-AMPA}} - I^i_{\text{GABA}} - I^{i,\ \text{stimulus}}_{inter\text{-AMPA}}, \tag{19}$$

DRAFT

In the context of the two-cortical-column model, the equations for the dynamics of the average membrane potential of each cortical population, $V_{p/i}$, as described by equation 14 and 15, can be expressed as follows:

$$\tau_p \dot{V}_p = -I_{\mathrm{L}}^p - I_{intra\text{-AMPA}}^p - I_{inter\text{-AMPA}}^p - I_{\mathrm{GABA}}^p - \tau_p C_m^{-1} I_{\mathrm{KNa}} - I_{inter\text{-AMPA}}^{p,\ \mathrm{stimulus}}, \quad \textbf{(20)}$$

$$\tau_i \dot{V}_i = -I_{\mathrm{L}}^i - I_{intra\text{-AMPA}}^i - I_{inter\text{-AMPA}}^p - I_{\mathrm{GABA}}^i - I_{inter\text{-AMPA}}^{i,\ \mathrm{stimulus}}, \quad \textbf{(21)}$$

Stimuli are depicted as boxcar functions, each lasting 100 milliseconds. Specifically, the variable $Q_{p^{um}}^{\mathrm{stimulus}}$ maintains a value of zero both before the stimulus onset and after the stimulus offset. In the context of the two-cortical-column model, one of the columns receives the stimuli directly, hereafter referred to as the *perturbed cortical column*. The other cortical column, which does not receive direct stimuli, is designated as the *unperturbed cortical column*. It is important to note that $Q_{p^{um}}^{\mathrm{stimulus}}$ remains at zero for the unperturbed cortical column, so does $I_{inter\text{-AMPA}}^{k,\ \mathrm{stimulus}}$, where k can represent either p' or i'.

Initially, we carry out a single noise-free trial in which the respective model is subjected to stimuli with increasing stimuli strength. This trial is designed to evaluate noise-free evoked responses for NREM sleep and various synaptic upscalings in wakefulness. Subsequently, we conduct 500 independent trials separately for NREM sleep and various synaptic upscalings in wakefulness within the corresponding model. These trials are intended to assess stochastic evoked responses.

Data Analysis

All data analyses were conducted offline using Python. Our analysis primarily focused on the firing rate signals generated by the pyramidal populations.

Analysis of Electrophysiological Patterns. In the first phase of each stage in the computational pipeline, we assessed the dynamic characteristics of spontaneous activities. This involved 500 independent trials for NREM sleep and synaptic upscalings in wakefulness (Fig. 1c(i)). Due to the symmetric connectivity paradigm in the two-cortical-column model, the analysis of spontaneous activities was confined to the pyramidal population in one of the cortical columns.

Analysis of amplitude-frequency content of firing rate signals. To assess the variability in the amplitude of spontaneous firing rate activities, we calculated the normalized distribution of firing rate signals for each brain state (NREM and various synaptic upscalings in wakefulness) separately, using a bin size of 1 mV (Fig. 1c(ii)).

To examine the variability in the frequency content of spontaneous firing rate activities, we generated spectrograms of firing rate signals for each brain state. This process involved segmenting each firing rate signal into 2-second intervals with a 90% overlap, assuming quasi-stationarity within each window (63). Each window was tapered using a Hann function to mitigate spectral leakage. We computed the Short-Time Fourier Transform (STFT) and derived the power spectral density (PSD) for each time window. Since the brain states were independently simulated and not time-locked events, we averaged the PSD over all time windows separately for each brain state (64). To quantify changes in each frequency band in the spectrogram, we normalized the PSD of each frequency band relative to the total PSD within each signal. The normalized PSD was, then, averaged over 500 trials (Fig. 1c(iii)).

Analysis of Evoked Responses to Stimuli.

Analysis of noise-free evoked responses. Noise-free evoked responses were assessed for both one- and two-cortical-column models subjected to stimuli with increasing strength. The amplitude of evoked firing responses was extracted at the stimulus offset subtracting the prestimulus values. These noise-free evoked responses provided insights into the influence of intra- and inter-synaptic upscaling on the amplitude of evoked responses, showcasing the *pulling* and *driving* effects, respectively (Fig. 2d(i),(ii)). This analysis was performed for NREM sleep and various synaptic upscaling configurations in wakefulness.

We also computed the synaptic excitation (E) and synaptic inhibition (I) on pyramidal populations for NREM sleep and various synaptic upscalings in wakefulness in both one- and two-cortical-column models. The E and I are defined as follows:

$$\mathrm{E} = I_{intra\text{-AMPA}}^k + I_{inter\text{-AMPA}}^k + I_{inter\text{-AMPA}}^{k,\ \mathrm{stimulus}}, \quad \textbf{(22)}$$

$$\mathrm{I} = I_{\mathrm{GABA}}^k, \quad \textbf{(23)}$$

where k is p in the one-cortical-column model and $k \in \{p,\ p'\}$ in the two-cortical-column model. Note that $I_{inter\text{-AMPA}}^k$ is zero in the one-cortical-column model and $I_{inter\text{-AMPA}}^{k,\ \mathrm{stimulus}}$ is zero for the unperturbed cortical column in the two-cortical-column model.

The E and I values were extracted from the noise-free simulations of the corresponding models. This approach was chosen because the average of this ratio computed in the stochastic condition will converge to the noise-free value for a sufficiently large number of trials. The net evoked synaptic current was quantified as $|\mathrm{E}| - |\mathrm{I}|$ (Extended Data Fig. 3).

Analysis of stochastic evoked responses. Stochastic evoked responses were assessed for both the one- and two-cortical-column models under various stimulus intensities. We conducted 500 independent trials for each stimulus intensity separately in the context of NREM sleep and all synaptic upscalings in wakefulness.

To evaluate the stochastic evoked firing responses, we developed a comprehensive framework for quantifying the information content in neural signals. This framework leverages various techniques, including machine learning methods, significance tests, and information theory, to estimate the information content within the stochastic evoked responses. We

DRAFT

applied this framework to assess the information content in the evoked firing responses at the stimulus offset.

Information Quantification. Neural firing can originate either spontaneously or as a response to an external stimulus. In a simplified model of hierarchical neural processing, a group of neurons (or a single neuron) responds to external stimuli by generating neural firing responses. These responses, in turn, influence the firing activity of postsynaptically connected neurons (or a single neuron), and so forth (65, 66). The neural spikes in the postsynaptic group contain information about the neural firing responses of the presynaptic group, which, in turn, holds information about the external stimuli. We define information from the perspective of a neuron as *"a difference that makes a difference"* (67). To quantify information in neural firing responses, we propose two measures: *information detection* and *information differentiation*.

Information detection. Information detection determines whether neural firing responses to a stimulus significantly differ from spontaneous neural firing. In essence, it assesses whether neural firing responses can be statistically attributed to the presentation of a stimulus. However, while information detection is essential for perception, it doesn't guarantee a high level of information about external stimuli encoded in neural firing responses. For example, if neural firing responses to two different stimuli each significantly differ from spontaneous neural firing activities but not significantly from each other, it indicates a lack of information to distinguish between stimuli. This does not imply a lack of information content but rather attenuated information content, as it can still distinguish neural firing responses from spontaneous activities.

Information differentiation. Information differentiation determines whether neural firing responses to different stimuli significantly differ from each other. It assesses whether neural firing responses can be statistically attributed to distinct stimuli. This measure is limited to the set of stimuli being tested. Information differentiation in neural firing responses can be high for a specific set of stimuli but may decrease with the introduction of new stimuli.

Information detection and differentiation together determine information content in neural firing responses. High levels of information detection and differentiation ensure accurate decoding of stimuli features from neural firing responses by an ideal observer with prior knowledge about the stimuli. Note that this framework for quantifying information content holds true for both spike-based and rate-based theories and whether neural coding is signal correlation or noise correlation.

Information propagation. Changes in information propagation between two neural groups in a hierarchical processing chain under different conditions can be quantified by measuring information content in each group. For instance, let's assume that information content in a presynaptic neural group is preserved in two different brain states. If information detection is preserved while differentiation is not in the postsynaptic neural group from one brain state to the other, it suggests that information content in the postsynaptic group is attenuated in the transition from one brain state to the other. It implies a reduced flow of information from the presynaptic to the postsynaptic group when the brain state switches. Changes in information detection and differentiation are not mutually exclusive; both can decrease in one brain state compared to another.

To quantify information detection and differentiation in a neural group, unsupervised and supervised machine learning algorithms can be utilized. Information detection is determined by how well a specific machine learning algorithm distinguishes between neural firing responses to a stimulus in poststimulus intervals and spontaneous neural firing activities in prestimulus intervals. Likewise, information differentiation is determined by how well a specific machine learning algorithm distinguishes among neural firing responses in poststimulus intervals to different stimuli. The Python module for information quantification, *iQuanta*, is available on GitHub (68).

Machine Learning Techniques.

Unsupervised framework. In the unsupervised framework, we employed the K-means clustering method to quantify information content in neural signals. The K-means clustering algorithm proceeded with three steps: identifying the number of clusters, estimating cluster centroids, and predictions.

To measure information detection, a K-means clustering method was derived separately for each stimulus intensity in NREM sleep and all synaptic upscalings in wakefulness to cluster the data, x. x represents the firing rate of the pyramidal population and consisted of 2×500 values (500 values for spontaneous firing activities and 500 values for evoked firing responses to a given stimulus intensity). We determined the number of clusters as two (for spontaneous and evoked clusters) and initialized corresponding cluster centroids randomly. Data were divided into training and test sets. The algorithm iteratively updated the cluster centroids using the training data and converged when centroids were stabilized. The trained cluster centroids were then used to predict the cluster label of data points in the test set (assigning each data point to the nearest cluster).

The performance of the clustering algorithm in predicting cluster labels was evaluated using Normalized Mutual Information (NMI) as an external validation technique, given access to the true labels (69). NMI measures the similarity between the predicted cluster labels, $C = \{C_1, C_2, \ldots, C_K\}$, and the true labels, $C' = \{C'_1, C'_2, \ldots, C'_{K'}\}$. Note that K and K' are equal to the number of clusters ($K = K' = 2$ for information detection). First, the mutual information between the predicted cluster labels and the true labels, $\mathrm{MI}(C, C')$, was computed as:

$$\mathrm{MI}(C, C') = \sum_{k=1}^{K} \sum_{k'=1}^{K'} p(k, k') \log_2 \frac{p(k, k')}{p(k)p(k')}, \qquad \textbf{(24)}$$

where $p(k)$ and $p(k')$ are, respectively, the probability of a

DRAFT

given data point belonging to C_k in clustering C and to $C'_{k'}$ in clustering C'. $p(k,k')$ is the joint probability of the given data point that belongs to C_k and $C'_{k'}$. $\mathrm{MI}(C,C')$ determines how much uncertainty is reduced about the true labels of data, C', by knowing predicted cluster labels, C, in the K-means clustering algorithm (70). Next, it is normalized to range between 0 and 1, indicating, respectively, no agreement and perfect agreement between the predicted and the true labels (69):

$$\mathrm{NMI}(C,C') = \frac{\mathrm{MI}(C,C')}{\sqrt{H(C)H(C')}}, \quad \textbf{(25)}$$

$$H(C) = -\sum_{k=1}^{K} p(k)\log_2 p(k), \quad \textbf{(26)}$$

where $H(C)$ and $H(C')$ are, respectively, the entropy associated with clustering C and C'. Higher NMI values indicate greater information detection.

To assess the effectiveness of the algorithm, we performed 10-fold cross-validation (71) and used stratified random sampling to eliminate the effect of data imbalances in training and test sets. Briefly, data were partitioned randomly into 10 subsets (folds) of equal size. Samples in all subsets except the first subset were used as the training set to estimate the cluster centroids. The held-out subset was used as the test set to estimate algorithm performance. The procedure repeated for all other subsets such that all subsets were used only once as the test set. The performance of the algorithm is then reported as the average over 10 performance estimates from the 10-fold cross-validation along with the 95% confidence interval (Fig. 3a).

To measure information differentiation, a K-means clustering method was derived separately in NREM sleep and all synaptic upscalings in wakefulness to cluster the data, x. x represents the firing rate of the pyramidal population and consisted of $N \times 500$ values, where N is the number of stimuli (500 values for evoked firing responses to each stimulus intensity). We determined the number of clusters as the number of stimuli, N. As in information detection, we used stratified 10-fold cross-validation to estimate cluster centroids and the performance of the algorithm. The NMI (see equation 25) was computed between the predicted cluster labels and the true labels on the test sets and was averaged over 10 performance estimates from the 10-fold cross-validation. Note that K and K' are equal to the number of stimulus intensities ($K = K' = N$ for information differentiation). Higher NMI values indicate greater information differentiation (Fig. 3c).

Supervised framework. In the supervised framework, we utilized the Generalized Linear Model (GLM) to quantify information content in neural signals. The GLM proceeded with three steps: model selection, estimation of model parameters, and prediction (72). Independent simulations across trials satisfied the assumption of independent observations in GLM.

To measure information detection, a GLM was derived separately for each stimulus intensity in NREM sleep and all synaptic upscalings in wakefulness. The GLM modeled the true distribution $q(y \mid x,\theta)$, where y represents the response variable (0 for absence of stimulus, 1 for presence of a given stimulus intensity), x represents the firing rate of the pyramidal population, and θ represent the model parameters. x consisted of 2×500 values (500 values for spontaneous firing activities and 500 values for evoked firing responses). We employed a Bernoulli distribution due to the binomial nature of the response variable. Stratified 10-fold cross-validation was used to asses the effectiveness of performance of the algorithm. A binomial logistic classification model was fitted on the training sets. The Newton-Raphson iterative optimization technique was carried out to optimize model parameters that maximize the log likelihood function (73, 74). Then, the trained model parameters were used to make predictions on the test sets. Model performance was evaluated using the classification accuracy score as the proportion of correctly predicted samples in the test sets (71). The classification accuracy score was averaged over 10 performance estimates from 10-fold cross-validation. The higher accuracy values indicate greater information detection (Extended Data Fig. 9a(i)).

To measure information differentiation, a GLM was derived separately for NREM sleep and all synaptic upscalings in wakefulness. It modeled the true distribution $q(y \mid x,\theta)$ with y representing the response variable with multiple values ($y \in 0,1,\ldots,N$ for N stimuli), x representing the firing rate of the pyramidal population, and θ representing the model parameters. x consisted of $N \times 500$ values, where N is the number of stimuli (500 values for evoked firing responses to each stimulus intensity). We used the multinomial distribution to estimate model parameters. Stratified 10-fold cross-validation was used to estimate model performance. The Newton-Raphson iterative optimization technique was carried out to optimize model parameters. The trained model parameters were used to estimate the model's performance on the test sets. The classification accuracy score on the test sets was averaged over 10 performance estimates. The higher accuracy values indicate greater information differentiation (Extended Data Fig. 9a(ii)).

Significance Tests and Information Theory.

Significance Test. In a departure from machine learning techniques, we conducted significance tests on firing rate signals from pyramidal populations.

To assess how significantly evoked responses at the stimulus offset differ from spontaneous activities during prestimulus intervals, we employed Student's t-test separately for various stimulus intensities in both NREM sleep and all synaptic upscalings in wakefulness. Given the large number of trials (500 trials), satisfying the conditions of the Central Limit Theorem, we computed the independent t-test statistic (t-value) as follows:

$$t = (\bar{x}_1 - \bar{x}_2)/(s\sqrt{2/n}), \quad \textbf{(27)}$$

$$s^2 = \frac{((n-1)s_1^2 + (n-1)s_2^2)}{2n-1}, \quad \textbf{(28)}$$

DRAFT

Here, $\bar{x}_1$ and $\bar{x}_2$ represent the averages across trials of evoked firing responses at the stimulus offset to a given stimulus intensity and spontaneous firing activities at a random time point in prestimulus intervals, respectively. n is the number of trials and $s^2_{1/2}$ is the variance of variable $x_{1/2}$ across trials. We set statistical significance at p-values below 0.05. The *t*-value was used as the measure to quantify the extent to which evoked responses differ from spontaneous activities. A higher *t*-value indicates greater information detection (Extended Data Fig. 9b(i)).

To assess how significantly evoked responses to different stimulus intensities are different from each other, we performed a one-way analysis of variance (ANOVA) separately in NREM sleep and all synaptic upscalings in wakefulness. We computed the F-ratio as follows:

$$\mathrm{F} = \frac{MS_B}{MS_W} \tag{29}$$

where MS_B and MS_W are between-group and within-group mean square values, respectively:

$$MS_B = \frac{\sum_{i=1}^{N} n(\bar{x}_i - \bar{x})}{N-1}, \tag{30}$$

$$MS_W = \frac{\sum_{i=1}^{N}\sum_{j=1}^{n}(x_{i,j} - \bar{x}_i)}{N(n-1)}, \tag{31}$$

Here, N represents the number of stimuli, and n is the number of trials. $\bar{x}_{i,j}$ is the evoked firing response to stimulus i in trial j, $\bar{x}_i$ is the average of $\bar{x}_{i,j}$ across trials, and $\bar{x}$ is the average of $\bar{x}_i$ across stimuli. The F-ratio was used as the measure to quantify how distinct evoked responses to different stimulus intensities are from each other. A higher F-ratio indicates greater information differentiation (Extended Data Fig. 9b(ii)).

Information Theory. Information theory was also employed to evaluate how informative evoked firing responses at the stimulus offset are about stimulus intensities. Mutual information measures the information about a stimulus in the probability distribution of firing rates, as follows (66):

$$I(X, s_j) = \sum_i p(x_i|s_j)\log_2 \frac{p(x_i|s_j)}{p(x_i)}, \tag{32}$$

Here, $I(X, s_j)$ represents the mutual information between the distribution of firing responses X and stimulus s_j. $p(x_i)$ and $p(x_i|s_j)$ are, respectively, the probability that firing responses take the value x_i and the conditional probability that firing responses take the value x_i for a given stimulus s_j. Summing values of mutual information for all stimuli results in a scalar mutual information value $I(X, S)$. A larger separation among the distributions of evoked responses to stimuli results in a larger mutual information value. Therefore, a larger mutual information value might represent a higher degree of information differentiation (Extended Data Fig. 9c). Note that to compute mutual information, we discretized firing rate signals into 0.1 Hz bins to calculate the probabilities.

Declarations

Supplementary information. The supplementary information for this paper includes the mathematical formalism for the computational models and extended data Figures.

Funding. This research was funded by the Postdoctoral Junior Leader Fellowship Programme from La Caixa Banking Foundation (LCF/BQ/PI18/11630004).

Competing interests. The authors declare no competing interests. The funders had no role in the design of the study; in the collection, analyses, or interpretation of data; in the writing of the manuscript, or in the decision to publish the results.

Ethics approval. Not applicable

Consent to participate. Not applicable

Consent for publication. Not applicable

Data availability. Not applicable

Code availability. Code supporting the findings of this paper are available on github (62, 68).

Authors' contributions. F.R. and B.S. conceived the research. B.S. secured funding. F.R. and B.S. developed the methodology. F.R. designed the simulations and carried out data curation, data analysis, and data visualization. F.R. wrote the original draft. F.R. and B.S. wrote and edited the manuscript. B.S. supervised the research.

Acknowledgment. We thank Francesco Damiani for comments on this manuscript.

DRAFT

Bibliography

1. Karl J. Friston. Functional and effective connectivity in neuroimaging: A synthesis. *Human Brain Mapping*, 2:56–78, 1994. doi: 10.1002/hbm.460020107.
2. Marcello Massimini, Fabio Ferrarelli, Reto Huber, Steve K. Esser, Harpreet Singh, and Giulio Tononi. Breakdown of cortical effective connectivity during sleep. *Science*, 309:2228–2232, 2005. doi: 10.1126/science.1117256.
3. Adenauer G. Casali, Olivia Gosseries, Mario Rosanova, Mélanie Boly, Simone Sarasso, Karina R. Casali, Silvia Casarotto, Marie-Aurélie Bruno, Steven Laureys, Giulio Tononi, and Marcello Massimini. A theoretically based index of consciousness independent of sensory processing and behavior. *Science Translational Medicine*, 5:198ra105–198ra105, 2013. doi: 10.1126/scitranslmed.3006294.
4. Hanna Hayat, Amit Marmelshtein, Aaron J. Krom, Yaniv Sela, Ariel Tankus, Ido Strauss, Firas Fahoum, Itzhak Fried, and Yuval Nir. Reduced neural feedback signaling despite robust neuron and gamma auditory responses during human sleep. *Nature Neuroscience*, 25:935–943, 2022. doi: 10.1038/s41593-022-01107-4.
5. Thomas E. Scammell, Elda Arrigoni, and Jonathan O. Lipton. Neural circuitry of wakefulness and sleep. *Neuron*, 93:747–765, 2017. doi: 10.1016/j.neuron.2017.01.014.
6. Mircea Steriade, David A. McCormick, and Terrence J. Sejnowski. Thalamocortical oscillations in the sleeping and aroused brain. *Science*, 262:679–685, 1993. doi: 10.1126/science.8235588.
7. M. Steriade, I. Timofeev, and F. Grenier. Natural waking and sleep states: A view from inside neocortical neurons. *Journal of Neurophysiology*, 85:1969–1985, 2001. doi: 10.1152/jn.2001.85.5.1969.
8. Chiara Cirelli and Giulio Tononi. Differential expression of plasticity-related genes in waking and sleep and their regulation by the noradrenergic system. *The Journal of Neuroscience*, 20:9187–9194, 2000. doi: 10.1523/jneurosci.20-24-09187.2000.
9. Giulio Tononi and Chiara Cirelli. Sleep function and synaptic homeostasis. *Sleep Medicine Reviews*, 10:49–62, 2006. doi: 10.1016/j.smrv.2005.05.002.
10. Giulio Tononi and Chiara Cirelli. Sleep and the price of plasticity: From synaptic and cellular homeostasis to memory consolidation and integration. *Neuron*, 81:12–34, 2014. doi: 10.1016/j.neuron.2013.12.025.

11. Marcello Massimini, Fabio Ferrarelli, Steve K. Esser, Brady A. Riedner, Reto Huber, Michael Murphy, Michael J. Peterson, and Giulio Tononi. Triggering sleep slow waves by transcranial magnetic stimulation. *Proceedings of the National Academy of Sciences*, 104:8496–8501, 2007. doi: 10.1073/pnas.0702495104.
12. Giulio Tononi and Marcello Massimini. Why does consciousness fade in early sleep?. *Annals of the New York Academy of Sciences*, 1129:330–334, 2008. doi: 10.1196/annals.1417.024.
13. Marcello Massimini, Fabio Ferrarelli, Simone Sarasso, and Giulio Tononi. Cortical mechanisms of loss of consciousness: insight from tms/eeg studies. *Archives italiennes de biologie*, 150:44–55, 2012. doi: 10.4449/aib.v150i2.1361.
14. Andrea Pigorini, Simone Sarasso, Paola Proserpio, Caroline Szymanski, Gabriele Arnulfo, Silvia Casarotto, Matteo Fecchio, Mario Rosanova, Maurizio Mariotti, Giorgio Lo Russo, J. Matias Palva, Lino Nobili, and Marcello Massimini. Bistability breaks-off deterministic responses to intracortical stimulation during non-REM sleep. *NeuroImage*, 112:105–113, 2015. doi: 10.1016/j.neuroimage.2015.02.056.
15. Elias B. Issa and Xiaoqin Wang. Sensory responses during sleep in primate primary and secondary auditory cortex. *The Journal of Neuroscience*, 28:14467–14480, 2008. doi: 10.1523/jneurosci.3086-08.2008.
16. Yuval Nir, Vladyslav V. Vyazovskiy, Chiara Cirelli, Matthew I. Banks, and Giulio Tononi. Auditory responses and stimulus-specific adaptation in rat auditory cortex are preserved across NREM and REM sleep. *Cerebral Cortex*, 25:1362–1378, 2013. doi: 10.1093/cercor/bht328.
17. Yaniv Sela, Vladyslav V. Vyazovskiy, Chiara Cirelli, Giulio Tononi, and Yuval Nir. Responses in rat core auditory cortex are preserved during sleep spindle oscillations. *Sleep*, 39:1069–1082, 2016. doi: 10.5665/sleep.5758.
18. Yaniv Sela, Aaron Joseph Krom, Lottem Bergman, Noa Regev, and Yuval Nir. Sleep differentially affects early and late neuronal responses to sounds in auditory and perirhinal cortices. *The Journal of Neuroscience*, 40:2895–2905, 2020. doi: 10.1523/jneurosci.1186-19.2020.
19. Julian M. Budd and Zoltán F. Kisvárday. Local lateral connectivity of inhibitory clutch cells in layer 4 of cat visual cortex (area 17). *Experimental Brain Research*, 140:245–250, 2001. doi: 10.1007/s002210100817.
20. Péter Buzás, Krisztina Kovács, Alex S. Ferecskó, Julian M.L. Budd, Ulf T. Eysel, and Zoltán F. Kisvárday. Model-based analysis of excitatory lateral connections in the visual cortex. *Journal of Comparative Neurology*, 499:861–881, 2006. doi: 10.1002/cne.21134.
21. Ján Antolík. Rapid long-range disynaptic inhibition explains the formation of cortical orientation maps. *Frontiers in Neural Circuits*, 11:21, 2017. doi: 10.3389/fncir.2017.00021.
22. Frances S Chance, L.F Abbott, and Alex D Reyes. Gain modulation from background synaptic input. *Neuron*, 35:773–782, 2002. doi: 10.1016/s0896-6273(02)00820-6.
23. R.W. Guillery and S.Murray Sherman. Thalamic relay functions and their role in corticocortical communication. *Neuron*, 33:163–175, 2002. doi: 10.1016/s0896-6273(01)00582-7.
24. Gordon M. G. Shepherd and Naoki Yamawaki. Untangling the cortico-thalamo-cortical loop: cellular pieces of a knotty circuit puzzle. *Nature Reviews Neuroscience*, 22:389–406, 2021. doi: 10.1038/s41583-021-00459-3.
25. Hugh R. Wilson and Jack D. Cowan. Excitatory and inhibitory interactions in localized populations of model neurons. *Biophysical Journal*, 12:1–24, 1972. doi: 10.1016/s0006-3495(72)86068-5.
26. Arne Weigenand, Michael Schellenberger Costa, Hong-Viet Victor Ngo, Jens Christian Claussen, and Thomas Martinetz. Characterization of k-complexes and slow wave activity in a neural mass model. *PLoS Computational Biology*, 10:e1003923, 2014. doi: 10.1371/journal.pcbi.1003923.
27. Farhad Razi, Rubén Moreno-Bote, and Belén Sancristóbal. Computational modeling of information propagation during the sleep–waking cycle. *Biology*, 10:945, 2021. doi: 10.3390/biology10100945.
28. Maria V. Sanchez-Vives and David A. McCormick. Cellular and network mechanisms of rhythmic recurrent activity in neocortex. *Nature Neuroscience*, 3:1027–1034, 2000. doi: 10.1038/79848.
29. Albert Compte, Maria V. Sanchez-Vives, David A. McCormick, and Xiao-Jing Wang. Cellular and network mechanisms of slow oscillatory activity ($<$1 hz) and wave propagations in a cortical network model. *Journal of Neurophysiology*, 89:2707–2725, 2003. doi: 10.1152/jn.00845.2002.
30. Vladyslav V. Vyazovskiy, Umberto Olcese, Yaniv M. Lazimy, Ugo Faraguna, Steve K. Esser, Justin C. Williams, Chiara Cirelli, and Giulio Tononi. Cortical firing and sleep homeostasis. *Neuron*, 63:865–878, 2009. doi: 10.1016/j.neuron.2009.08.024.
31. Maria V Sanchez-Vives. Origin and dynamics of cortical slow oscillations. *Current Opinion in Physiology*, 15:217–223, 2020. doi: 10.1016/j.cophys.2020.04.005.
32. G. Moruzzi and H.W. Magoun. Brain stem reticular formation and activation of the eeg. *Electroencephalography and Clinical Neurophysiology*, 1:455–473, 1949. doi: 10.1016/0013-4694(49)90219-9.
33. G Aston-Jones, C Chiang, and T Alexinsky. Discharge of noradrenergic locus coeruleus neurons in behaving rats and monkeys suggests a role in vigilance. *Progress in brain research*, 88:501–520, 1991. doi: 10.1016/s0079-6123(08)63830-3.
34. Madhura R. Joglekar, Jorge F. Mejias, Guangyu Robert Yang, and Xiao-Jing Wang. Interareal balanced amplification enhances signal propagation in a large-scale circuit model of the primate cortex. *Neuron*, 98:222–234.e8, 2018. doi: 10.1016/j.neuron.2018.02.031.
35. Gustavo Deco, Yonathan Sanz Perl, Peter Vuust, Enzo Tagliazucchi, Henry Kennedy, and Morten L. Kringelbach. Rare long-range cortical connections enhance human information processing. *Current Biology*, 31:4436–4448.e5, 2021. doi: 10.1016/j.cub.2021.07.064.
36. Leslie D Claar, Irene Rembado, Jacqulyn R Kuyat, Simone Russo, Lydia C Marks, Shawn R Olsen, and Christof Koch. Cortico-thalamo-cortical interactions modulate electrically evoked EEG responses in mice. *eLife*, 12:RP84630, 2023. doi: 10.7554/elife.84630.3.
37. David A. McCormick. Cholinergic and noradrenergic modulation of thalamocortical processing. *Trends in Neurosciences*, 12:215–221, 1989. doi: 10.1016/0166-2236(89)90125-2.
38. David A McCormick and Thierry Bal. Sensory gating mechanisms of the thalamus. *Current Opinion in Neurobiology*, 4:550–556, 1994. doi: 10.1016/0959-4388(94)90056-6.
39. S. Murray Sherman and R. W. Guillery. The role of the thalamus in the flow of information to the cortex. *Philosophical Transactions of the Royal Society of London. Series B: Biological Sciences*, 357:1695–1708, 2002. doi: 10.1098/rstb.2002.1161.
40. Ian Oswald, Anne M. Taylor, and Michel Treisman. Discriminative responses to stimulation during human sleep. *Brain*, 83:440–453, 1960. doi: 10.1093/brain/83.3.440.
41. Thomas Andrillon, Andreas Trier Poulsen, Lars Kai Hansen, Damien Léger, and Sid Kouider. Neural markers of responsiveness to the environment in human sleep. *The Journal of Neuroscience*, 36:6583–6596, 2016. doi: 10.1523/jneurosci.0902-16.2016.
42. Guillaume Legendre, Thomas Andrillon, Matthieu Koroma, and Sid Kouider. Sleepers track informative speech in a multitalker environment. *Nature Human Behaviour*, 3:274–283, 2019. doi: 10.1038/s41562-018-0502-5.
43. F Perrin. A differential brain response to the subject's own name persists during sleep. *Clinical Neurophysiology*, 110:2153–2164, 1999. doi: 10.1016/s1388-2457(99)00177-7.
44. Chiara Cirelli and Giulio Tononi. Effects of sleep and waking on the synaptic ultrastructure. *Philosophical Transactions of the Royal Society B: Biological Sciences*, 375:20190235, 2020. doi: 10.1098/rstb.2019.0235.
45. J J Hopfield. Neural networks and physical systems with emergent collective computational abilities. *Proceedings of the National Academy of Sciences*, 79:2554–2558, 1982. doi: 10.1073/pnas.79.8.2554.
46. Mark S. Cembrowski and Nelson Spruston. Heterogeneity within classical cell types is the rule: lessons from hippocampal pyramidal neurons. *Nature Reviews Neuroscience*, 20:193–204, 2019. doi: 10.1038/s41583-019-0125-5.
47. Hannah Monyer, Nail Burnashev, David J. Laurie, Bert Sakmann, and Peter H. Seeburg. Developmental and regional expression in the rat brain and functional properties of four NMDA receptors. *Neuron*, 12:529–540, 1994. doi: 10.1016/0896-6273(94)90210-0.
48. J. F. Mejias and A. Longtin. Optimal heterogeneity for coding in spiking neural networks. *Physical Review Letters*, 108:228102, 2012. doi: 10.1103/physrevlett.108.228102.
49. Fleur Zeldenrust, Boris Gutkin, and Sophie Denéve. Efficient and robust coding in heterogeneous recurrent networks. *PLOS Computational Biology*, 17:e1008673, 2021. doi: 10.1371/journal.pcbi.1008673.
50. Scott Rich, Homeira Moradi Chameh, Jeremie Lefebvre, and Taufik A. Valiante. Loss of neuronal heterogeneity in epileptogenic human tissue impairs network resilience to sudden changes in synchrony. *Cell Reports*, 39:110863, 2022. doi: 10.1016/j.celrep.2022.110863.
51. Nicolas Perez-Nieves, Vincent C. H. Leung, Pier Luigi Dragotti, and Dan F. M. Goodman. Neural heterogeneity promotes robust learning. *Nature Communications*, 12:5791, 2021. doi: 10.1038/s41467-021-26022-3.
52. Olivier David and Karl J. Friston. A neural mass model for MEG/EEG:. *NeuroImage*, 20:1743–1755, 2003. doi: 10.1016/j.neuroimage.2003.07.015.
53. Steve K. Esser, Sean Hill, and Giulio Tononi. Breakdown of effective connectivity during slow wave sleep: Investigating the mechanism underlying a cortical gate using large-scale modeling. *Journal of Neurophysiology*, 102:2096–2111, 2009. doi: 10.1152/jn.00059.2009.
54. G. Deco, A. Ponce-Alvarez, P. Hagmann, G. L. Romani, D. Mantini, and M. Corbetta. How local excitation-inhibition ratio impacts the whole brain dynamics. *Journal of Neuroscience*, 34:7886–7898, 2014. doi: 10.1523/jneurosci.5068-13.2014.
55. Benjamin P. Cohen, Carson C. Chow, and Shashaank Vattikuti. Dynamical modeling of multi-scale variability in neuronal competition. *Communications Biology*, 2:319, 2019. doi: 10.1038/s42003-019-0555-7.
56. Almudena Barbero-Castillo, Pedro Mateos-Aparicio, Leonardo Dalla Porta, Alessandra Camassa, Lorena Perez-Mendez, and Maria V. Sanchez-Vives. Impact of $GABA_a$ and $GABA_b$ inhibition on cortical dynamics and perturbational complexity during synchronous and desynchronized states. *The Journal of Neuroscience*, 41:5029–5044, 2021. doi: 10.1523/jneurosci.1837-20.2021.
57. Jennifer S. Goldman, Lionel Kusch, David Aquilue, Bahar Hazal Yalçınkaya, Damien Depannemaecker, Kevin Ancourt, Trang-Anh E. Nghiem, Viktor Jirsa, and Alain Destexhe. A comprehensive neural simulation of slow-wave sleep and highly responsive wakefulness dynamics. *Frontiers in Computational Neuroscience*, 16:1058957, 2023. doi: 10.3389/fncom.2022.1058957.
58. Wulfram Gerstner, Werner M Kistler, Richard Naud, and Liam Paninski. *Neuronal dynamics: From single neurons to networks and models of cognition*. Cambridge University Press, Cambridge, 2014.
59. A. L. Hodgkin, A. F. Huxley, and B. Katz. Measurement of current-voltage relations in the membrane of the giant axon of $loligo$. *The Journal of Physiology*, 116:424–448, 1952. doi: 10.1113/jphysiol.1952.sp004716.
60. Alain Destexhe, Stuart W. Hughes, Michelle Rudolph, and Vincenzo Crunelli. Are corticothalamic 'up' states fragments of wakefulness? *Trends in Neurosciences*, 30:334–342, 2007. doi: 10.1016/j.tins.2007.04.006.
61. Maxi San Miguel and Raúl Toral. Stochastic effects in physical systems. In *Instabilities and Nonequilibrium Structures VI*, volume 5, pages 35–127, Dordrecht, 2000. Springer.
62. Farhad Razi. Simulation routine of the model, 2024. Available online: https://github.com/fraziphy/heterogeneous_synaptic_homeostasis [Accessed: 03/07/2024].
63. Walter Freeman and Rodrigo Quian Quiroga. *Imaging brain function with EEG: advanced temporal and spatial analysis of electroencephalographic signals*. Springer Science & Business Media, New York, 2013.
64. P. Welch. The use of fast fourier transform for the estimation of power spectra: A method based on time averaging over short, modified periodograms. *IEEE Transactions on Audio and Electroacoustics*, 15:70–73, 1967. doi: 10.1109/tau.1967.1161901.
65. Wulfram Gerstner, Andreas K. Kreiter, Henry Markram, and Andreas V. M. Herz. Neural codes: Firing rates and beyond. *Proceedings of the National Academy of Sciences*, 94:12740–12741, 1997. doi: 10.1073/pnas.94.24.12740.
66. Alexander Borst and Frédéric E. Theunissen. Information theory and neural coding. *Nature Neuroscience*, 2:947–957, 1999. doi: 10.1038/14731.
67. Giulio Tononi, Melanie Boly, Marcello Massimini, and Christof Koch. Integrated information theory: from consciousness to its physical substrate. *Nature Reviews Neuroscience*, 17:450–461, 2016. doi: 10.1038/nrn.2016.44.
68. Farhad Razi. Information quantification, 2024. Available online: https://github.com/fraziphy/iQuanta [Accessed: 03/07/2024].
69. Alexander Strehl and Joydeep Ghosh. Cluster ensembles—a knowledge reuse framework

DRAFT

for combining multiple partitions. *Journal of machine learning research*, 3:583–617, 2002. doi: 10.1162/153244303321897735.
70. Marina Meilă. Comparing clusterings—an information based distance. *Journal of Multivariate Analysis*, 98:873–895, 2007. doi: 10.1016/j.jmva.2006.11.013.
71. Max Kuhn and Kjell Johnson. *Applied predictive modeling*. Springer, New York, 2013.
72. P. McCullagh and J.A. Nelder. *Generalized Linear Models*. Routledge, London, 1983.
73. Christopher M Bishop and Nasser M Nasrabadi. *Pattern recognition and machine learning*. Springer, New York, 2006.
74. Stephen P Boyd and Lieven Vandenberghe. *Convex optimization*. Cambridge university press, Cambridge, 2004.

DRAFT

The mathematical formalism for the computational model has been previously described (27).

One-Cortical-Column Model. The one-cortical-column model consists of one pyramidal and one inhibitory population. The model utilizes the mathematical formalism of the Hodgkin-Huxley model to describe the membrane voltage activity in terms of driving synaptic activity. The synaptic activity contains one leak, two synaptic (intra-AMPAergic and GABAergic) currents, and one activity-dependent potassium current.

In the absence of Gaussian noise for the set of parameters in Table 2, the system relaxes to the steady-state solution. However, at every time point, the Gaussian noise disrupts the system from the steady-state solution. Nevertheless, the aforementioned synaptic currents drive the system back to the steady-state solution.

The full model equations for the one-cortical-column model are described by:

$$\begin{aligned}
\tau_p \dot{V}_p &= -I_{\mathrm{L}}^p - I_{intra\text{-AMPA}}^p - I_{\mathrm{GABA}}^p - \tau_p C_m^{-1} I_{\mathrm{KNa}}, \\
\tau_i \dot{V}_i &= -I_{\mathrm{L}}^i - I_{intra\text{-AMPA}}^i - I_{\mathrm{GABA}}^i,
\end{aligned}$$

$$\begin{aligned}
\ddot{s}_{pp} &= \gamma_p^2 \left(N_{pp}\, Q_p(V_p) + \phi_p - s_{pp}\right) - 2\gamma_p\, \dot{s}_{pp}, \\
\ddot{s}_{pi} &= \gamma_i^2 \left(N_{pi}\, Q_i(V_i) - s_{pi}\right) - 2\gamma_i\, \dot{s}_{pi}, \\
\ddot{s}_{ip} &= \gamma_p^2 \left(N_{ip}\, Q_p(V_p) + \phi_i - s_{ip}\right) - 2\gamma_p\, \dot{s}_{ip}, \\
\ddot{s}_{ii} &= \gamma_i^2 \left(N_{ii}\, Q_i(V_i) - s_{ii}\right) - 2\gamma_i\, \dot{s}_{ii},
\end{aligned}$$

$$\tau_{\mathrm{Na}}\, [\dot{\mathrm{N}}\mathrm{a}] = \alpha_{\mathrm{Na}} Q_p(V_p) - \mathrm{Na}_{\mathrm{pump}}([\mathrm{Na}]),$$

with the currents defined by:

$$\begin{aligned}
I_{\mathrm{L}}^k &= \bar{g}_{\mathrm{L}}(V_k - E_{\mathrm{L}}^k), \\
I_{\mathrm{AMPA}}^k &= \beta_{\mathrm{intra}}\, \bar{g}_{\mathrm{AMPA}} s_{kp}(V_k - E_{\mathrm{AMPA}}), \\
I_{\mathrm{GABA}}^k &= \beta_{\mathrm{GABA}}^k\, \bar{g}_{\mathrm{GABA}} s_{ki}(V_k - E_{\mathrm{GABA}}), \\
I_{\mathrm{KNa}} &= \bar{g}_{\mathrm{KNa}} \frac{0.37}{1 + (\frac{38.7}{[\mathrm{Na}]})^{3.5}} (V_p - E_{\mathrm{K}}),\ \textit{for}\ k \in \{p,\ i\},
\end{aligned}$$

The sodium pump and the firing rate functions are given by:

$$\begin{aligned}
\mathrm{Na}_{\mathrm{pump}}([\mathrm{Na}]) &= R_{\mathrm{pump}} \left(\frac{[\mathrm{Na}]^3}{[\mathrm{Na}]^3 + 3375} - \frac{[\mathrm{Na}]_{\mathrm{eq}}^3}{[\mathrm{Na}]_{\mathrm{eq}}^3 + 3375} \right), \\
Q_k(V_k) &= Q_k^{max} \frac{(1 + \tanh(C(V_k - \theta_k)/\sigma_k))}{2}, \quad C = \frac{\pi}{2\sqrt{3}},\ \textit{for}\ k \in \{p,\ i\},
\end{aligned}$$

Dynamical Constrains on β_{GABA}^k in the One-Cortical-Column Model. Upscaling the average conductance of intra-excitatory connections by a factor β_{intra} allows us to transition the model from NREM sleep dynamics to wakefulness, in agreement with SHY. To counterbalance the overexcitation each population receives due to intra-synaptic upscaling, the average GABAergic conductance on pyramidal and inhibitory populations is increased by a factor β_{GABA}^k, where $k \in \{p,\ i\}$. To do so, we use the peaks of V_p and V_i values during Up states in NREM sleep as the steady-state value of the average membrane potential of pyramidal and inhibitory populations in wakefulness. β_{GABA}^k is increased until the value of V_k (where $k \in \{p,\ i\}$) is obtained for various intra-synaptic upscalings in wakefulness.

The steady-state solution of the model equations in the one-cortical-column model (see Appendix) is obtained by setting the derivative of all variables to zero:

DRAFT

$$
\begin{aligned}
0 &= -I_{\mathrm{L}}^{p} - I_{intra\text{-AMPA}}^{p} - I_{\mathrm{GABA}}^{p} - \tau_p C_m^{-1} I_{\mathrm{KNa}}, \\
0 &= -I_{\mathrm{L}}^{i} - I_{intra\text{-AMPA}}^{i} - I_{\mathrm{GABA}}^{i}, \\
s_{kk'} &= N_{kk'}\, Q_{k'}(V_{k'}), \\
[\mathrm{Na}] &= \sqrt[3]{\frac{\mathrm{A}\cdot 3375}{1-\mathrm{A}}}, \\
\mathrm{A} &= \frac{\alpha_{\mathrm{Na}}}{R_{\mathrm{pump}}} Q_p(V_p) + \frac{[\mathrm{Na}]_{\mathrm{eq}}^3}{[\mathrm{Na}]_{\mathrm{eq}}^3 + 3375},
\end{aligned}
$$

Therefore, $\beta_{\mathrm{GABA}}^{k}$, $k \in \{p,\ i\}$ is as follows:

$$
\beta_{\mathrm{GABA}}^{p} = \frac{-\bar{g}_{\mathrm{L}}(V_p - E_{\mathrm{L}}^{p}) - \beta_{\mathrm{intra}}\, \bar{g}_{\mathrm{AMPA}}\, s_{pp}(V_p - E_{\mathrm{AMPA}})}{\bar{g}_{\mathrm{GABA}}\, s_{pi}(V_p - E_{\mathrm{GABA}})}
$$

$$
+ \frac{-\bar{g}_{\mathrm{KNa}}\, \dfrac{0.37}{1 + (\frac{38.7}{[\mathrm{Na}]})^{3.5}}\, (V_p - E_{\mathrm{K}})}{\bar{g}_{\mathrm{GABA}}\, s_{pi}(V_p - E_{\mathrm{GABA}})},
$$

$$
\beta_{\mathrm{GABA}}^{i} = \frac{-\bar{g}_{\mathrm{L}}(V_i - E_{\mathrm{L}}^{i}) - \beta_{\mathrm{intra}}\, \bar{g}_{\mathrm{AMPA}} s_{ip}(V_i - E_{\mathrm{AMPA}})}{\bar{g}_{\mathrm{GABA}}\, s_{ii}(V_i - E_{\mathrm{GABA}})},
$$

$\beta_{\mathrm{GABA}}^{k}$, where $k \in \{p,\ i\}$, for a given intra-synaptic upscaling in wakefulness is obtained by substituting the corresponding β_{intra} and the peaks of V_p and V_i values during Up states in NREM sleep.

Two-Cortical-Column Model. The two-cortical-column model consists of two cortical columns each containing one pyramidal and one inhibitory population (Appendix) that are mutually coupled through inter-excitatory connections. Full model equations for the two-cortical-column model are described by:

DRAFT

$$
\begin{aligned}
\tau_p \dot{V}_p &= -I^p_{\text{L}} - I^p_{intra\text{-AMPA}} - I^p_{inter\text{-AMPA}} - I^p_{\text{GABA}} - \tau_p C_m^{-1} I^p_{\text{KNa}}, \\
\tau_i \dot{V}_i &= -I^i_{\text{L}} - I^i_{intra\text{-AMPA}} - I^i_{inter\text{-AMPA}} - I^i_{\text{GABA}},
\end{aligned}
$$

$$
\begin{aligned}
\tau_{p'} \dot{V}_{p'} &= -I^{p'}_{\text{L}} - I^{p'}_{intra\text{-AMPA}} - I^{p'}_{inter\text{-AMPA}} - I^{p'}_{\text{GABA}} - \tau_{p'} C_m^{-1} I^{p'}_{\text{KNa}}, \\
\tau_{i'} \dot{V}_{i'} &= -I^{i'}_{\text{L}} - I^{i'}_{intra\text{-AMPA}} - I^{i'}_{inter\text{-AMPA}} - I^{i'}_{\text{GABA}},
\end{aligned}
$$

$$
\begin{aligned}
\ddot{s}_{pp} &= \gamma_p^2 \left(N_{pp}\, Q_p(V_p) + \phi_p - s_{pp} \right) - 2\gamma_p\, \dot{s}_{pp}, \\
\ddot{s}_{pi} &= \gamma_i^2 \left(N_{pi}\, Q_i(V_i) - s_{pi} \right) - 2\gamma_i\, \dot{s}_{pi}, \\
\ddot{s}_{ip} &= \gamma_p^2 \left(N_{ip}\, Q_p(V_p) + \phi_i - s_{ip} \right) - 2\gamma_p\, \dot{s}_{ip}, \\
\ddot{s}_{ii} &= \gamma_i^2 \left(N_{ii}\, Q_i(V_i) - s_{ii} \right) - 2\gamma_i\, \dot{s}_{ii},
\end{aligned}
$$

$$
\begin{aligned}
\ddot{s}_{p'p'} &= \gamma_{p'}^2 \left(N_{p'p'}\, Q_{p'}(V_{p'}) + \phi_{p'} - s_{p'p'} \right) - 2\gamma_{p'}\, \dot{s}_{p'p'}, \\
\ddot{s}_{p'i'} &= \gamma_{i'}^2 \left(N_{p'i'}\, Q_{i'}(V_{i'}) - s_{p'i'} \right) - 2\gamma_{i'}\, \dot{s}_{p'i'}, \\
\ddot{s}_{i'p'} &= \gamma_{p'}^2 \left(N_{i'p'}\, Q_{p'}(V_{p'}) + \phi_{i'} - s_{i'p'} \right) - 2\gamma_{p'}\, \dot{s}_{i'p'}, \\
\ddot{s}_{i'i'} &= \gamma_{i'}^2 \left(N_{i'i'}\, Q_{i'}(V_{i'}) - s_{i'i'} \right) - 2\gamma_{i'}\, \dot{s}_{i'i'},
\end{aligned}
$$

$$
\begin{aligned}
\ddot{s}_{pp'} &= \gamma_{p'}^2 \left(N_{pp'}\, Q_{p'}(V_{p'}) - s_{pp'} \right) - 2\gamma_{p'}\, \dot{s}_{pp'}, \\
\ddot{s}_{ip'} &= \gamma_{p'}^2 \left(N_{ip'}\, Q_{p'}(V_{p'}) - s_{ip'} \right) - 2\gamma_{p'}\, \dot{s}_{ip'},
\end{aligned}
$$

$$
\begin{aligned}
\ddot{s}_{p'p} &= \gamma_p^2 \left(N_{p'p}\, Q_p(V_p) - s_{p'p} \right) - 2\gamma_p\, \dot{s}_{p'p}, \\
\ddot{s}_{i'p} &= \gamma_p^2 \left(N_{i'p}\, Q_p(V_p) - s_{i'p} \right) - 2\gamma_p\, \dot{s}_{i'p},
\end{aligned}
$$

$$
\begin{aligned}
\tau_{\text{Na}}\, [\dot{\text{Na}}]_p &= \alpha_{\text{Na}} Q_p(V_p) - \text{Na}_{\text{pump}}([\text{Na}]_p), \\
\tau_{\text{Na}}\, [\dot{\text{Na}}]_{p'} &= \alpha_{\text{Na}} Q_{p'}(V_{p'}) - \text{Na}_{\text{pump}}([\text{Na}]_{p'}),
\end{aligned}
$$

where I^h_{KNa} is the sodium-dependent potassium current of the pyramidal population either in the first and second cortical column, $h \in \{p, p'\}$. The currents are defined by:

$$
I^k_{\text{L}} = \bar{g}_{\text{L}}(V_k - E^k_{\text{L}}), \textit{for } k \in \{p,\ i,\ p',\ i'\},
$$

$$
\begin{aligned}
I^k_{intra\text{-AMPA}} &= \beta_{\text{intra}}\, \bar{g}_{\text{AMPA}}\, s_{kp}\, (V_k - E_{\text{AMPA}}) \\
I^k_{inter\text{-AMPA}} &= \beta_{\text{inter}}\, \bar{g}_{\text{AMPA}}\, s_{kp'}\, (V_k - E_{\text{AMPA}}) \\
I^k_{\text{GABA}} &= \beta^k_{\text{GABA}}\, \bar{g}_{\text{GABA}} s_{ki} (V_k - E_{\text{GABA}}), \textit{for } k \in \{p,\ i\},
\end{aligned}
$$

$$
\begin{aligned}
I^k_{intra\text{-AMPA}} &= \beta_{\text{intra}}\, \bar{g}_{\text{AMPA}}\, s_{kp'}\, (V_k - E_{\text{AMPA}}) \\
I^k_{inter\text{-AMPA}} &= \beta_{\text{inter}}\, \bar{g}_{\text{AMPA}}\, s_{kp}\, (V_k - E_{\text{AMPA}}) \\
I^k_{\text{GABA}} &= \beta^k_{\text{GABA}}\, \bar{g}_{\text{GABA}} s_{ki'} (V_k - E_{\text{GABA}}), \textit{for } k \in \{p',\ i'\},
\end{aligned}
$$

$$
I^h_{\text{KNa}} = \bar{g}_{\text{KNa}}\, \frac{0.37}{1 + (\frac{38.7}{[\text{Na}]_h})^{3.5}}\, (V_h - E_{\text{K}}), \textit{for } h \in \{p,\ p'\},
$$

The sodium pump and firing rate functions are given by:

DRAFT

$$\mathrm{Na}_{\mathrm{pump}}([\mathrm{Na}]_h) = R_{\mathrm{pump}}\left(\frac{[\mathrm{Na}]_h^3}{[\mathrm{Na}]_h^3+3375} - \frac{[\mathrm{Na}]_{\mathrm{eq}}^3}{[\mathrm{Na}]_{\mathrm{eq}}^3+3375}\right), \textit{for } h \in \{p,\, p'\},$$

$$Q_k(V_k) = Q_k^{max}\,\frac{(1+\tanh(C(V_k-\theta_k)/\sigma_k))}{2}, \quad C = \frac{\pi}{2\sqrt{3}}, \textit{for } k \in \{p,\, i,\, p',\, i'\},$$

Dynamical Constrains on β^k_{GABA} in the Two-Cortical-Column Model. Inter-excitatory connections introduce overexcitation to the pyramidal and inhibitory populations in NREM sleep. To keep the steady-state value of V_p and V_i in the two-cortical-column model equal to the ones in the one-cortical-column model in NREM sleep, β^k_{GABA}, where $k \in \{p,\, i,\, p',\, i'\}$, is increased to counterbalance the the effects of inter-excitatory connections. The same procedure is carried out for all synaptic upscalings in wakefulness, except that the values of V_p and V_i during Up state in NREM sleep in the one-cortical-column model is used. The steady-state solution of the model equations for the two-cortical-column (see Appendix) is obtained by setting the derivatives of all variables to zero:

$$\begin{aligned}
0 &= -I_{\mathrm{L}}^{p/p'} - I_{\mathrm{AMPA}}^{p/p'} - I_{\mathrm{GABA}}^{p/p'} - \tau_{p/p'} C_m^{-1} I_{\mathrm{KNa}}^{p/p'},\\
0 &= -I_{\mathrm{L}}^{i/i'} - I_{\mathrm{AMPA}}^{i/i'} - I_{\mathrm{GABA}}^{i/i'},\\
s_{kk'} &= N_{kk'}\, Q_{k'}(V_{k'}),\\
s_{kk'} &= N_{kk'}\, Q_{k'}(V_{k'})\\
[\mathrm{Na}]_{p/p'} &= \sqrt[3]{\frac{\mathrm{A}_{p/p'}\cdot 3375}{1-\mathrm{A}_{p/p'}}},\\
\mathrm{A}_{p/p'} &= \frac{\alpha_{\mathrm{Na}}}{R_{\mathrm{pump}}} Q_{p/p'}(V_{p/p'}) + \frac{[\mathrm{Na}]_{\mathrm{eq}}^3}{[\mathrm{Na}]_{\mathrm{eq}}^3+3375},
\end{aligned}$$

By taking into account the symmetry between the two cortical columns, we set the steady-state value of V_p equal to $V_{p'}$ and V_i equal to $V_{i'}$ ($V_{p'} = V_p$ and $V_{i'} = V_i$). Therefore, to keep the average membrane potential of pyramidal and inhibitory populations in the two-cortical-column model equal to the ones in the one-cortical-column model both during NREM sleep and wakefulness, β^k_{GABA}, where $k \in \{p,\, i,\, p',\, i'\}$, changes as follows:

$$\begin{aligned}
\beta_{\mathrm{GABA}}^{p/p'} = &\frac{-\bar{g}_{\mathrm{L}}(V_p - E_{\mathrm{L}}^p) - \beta_{\mathrm{intra}}\, \bar{g}_{\mathrm{AMPA}}\, s_{pp}(V_p - E_{\mathrm{AMPA}})}{\bar{g}_{\mathrm{GABA}}\, s_{pi}(V_p - E_{\mathrm{GABA}})}\\
&+ \frac{-\beta_{\mathrm{inter}}\, \bar{g}_{\mathrm{AMPA}}\, s_{pp'}(V_p - E_{\mathrm{AMPA}})}{\bar{g}_{\mathrm{GABA}}\, s_{pi}(V_p - E_{\mathrm{GABA}})}\\
&+ \frac{-\bar{g}_{\mathrm{KNa}}\, \frac{0.37}{1+(\frac{38.7}{[\mathrm{Na}]})^{3.5}}\,(V_p - E_{\mathrm{K}})}{\bar{g}_{\mathrm{GABA}}\, s_{pi}(V_p - E_{\mathrm{GABA}})},
\end{aligned}$$

$$\begin{aligned}
\beta_{\mathrm{GABA}}^{i/i'} = &\frac{-\bar{g}_{\mathrm{L}}(V_i - E_{\mathrm{L}}^i) - \beta_{\mathrm{intra}}\, \bar{g}_{\mathrm{AMPA}} s_{ip}(V_i - E_{\mathrm{AMPA}})}{\bar{g}_{\mathrm{GABA}}\, s_{ii}(V_i - E_{\mathrm{GABA}})}\\
&+ \frac{-\beta_{\mathrm{inter}}\, \bar{g}_{\mathrm{AMPA}}\, s_{ip'}(V_i - E_{\mathrm{AMPA}})}{\bar{g}_{\mathrm{GABA}}\, s_{ii}(V_i - E_{\mathrm{GABA}})},
\end{aligned}$$

β^k_{GABA}, where $k \in \{p,\, i,\, p',\, i'\}$, during NREM sleep in the two-cortical-column model is obtained by setting $\beta_{\mathrm{intra}} = \beta_{\mathrm{inter}} = 1$ and using the steady-state values of V_p and V_i in NREM sleep from the one-cortical-column model.

DRAFT

β^k_{GABA}, where $k \in \{p,\, i,\, p',\, i'\}$, for a given synaptic upscaling during wakefulness in the two-cortical-column model is obtained by substituting the corresponding β_{intra} and β_{inter} values and the peaks of V_p and V_i during Up states in NREM sleep from the one-cortical-column model.

DRAFT

Extended Data Figures

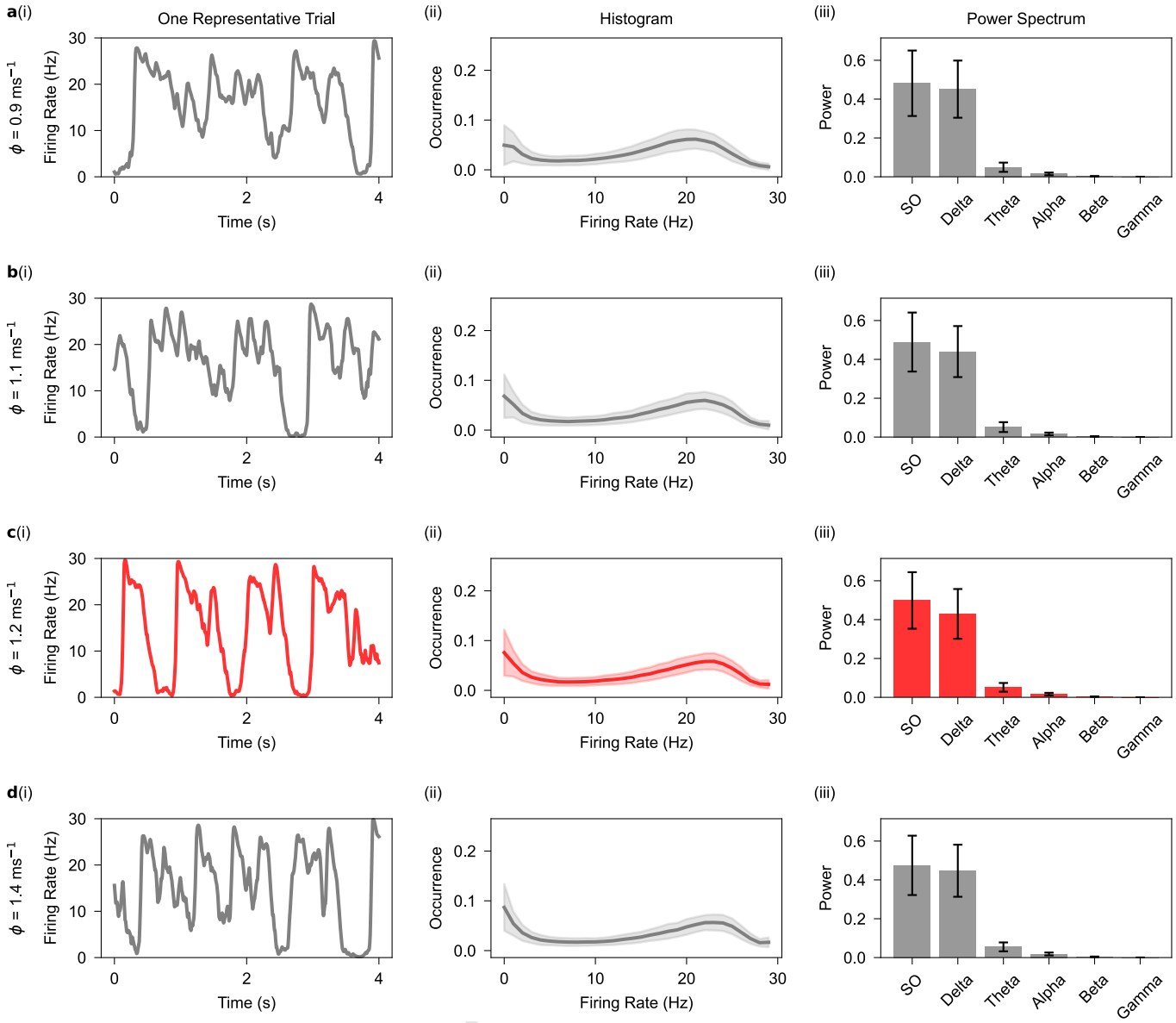

Extended Data Fig. 1. Dynamical features of spontaneous firing activity in the one-cortical-column model are robust to the changes in the standard deviation of the noise, ϕ. **a**, Spontaneous firing rate signal for a representative trial (i), the distribution of firing rate signals (ii), and the power spectrum of signals (iii) when $\phi = 0.9$ ms^{-1}. **b**, **c**, and **d**, As in **a**, but for when ϕ increases. Panel **c** here is as Fig. 1**c**. Note that $\phi = 1.2$ ms^{-1} is used as the value of the standard deviation of the noise in this computational study. Shaded area and Error bar correspond to standard deviation over 500 trials.

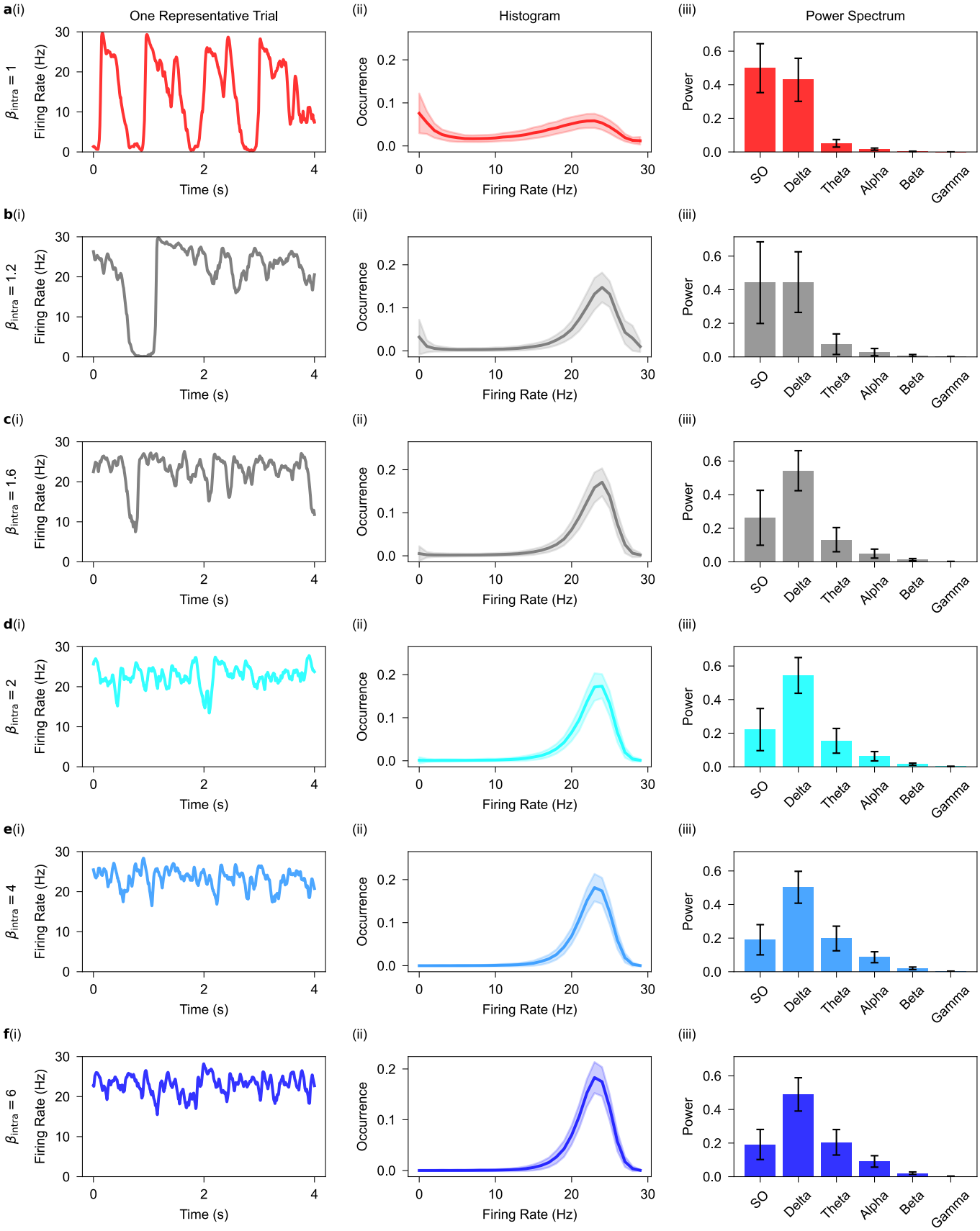

Extended Data Fig. 2. Dynamical features of spontaneous firing activity in the one-cortical-column model changes with increasing intra-synaptic upscaling, β_{intra}. **a**, Spontaneous firing rate signal for a representative trial (i), the distribution of firing rate signals (ii), and the power spectrum of signals (iii) when there is no intra-synaptic upscaling ($\beta_{\text{intra}} = 1$). Panel **a** here is as Fig. 1**c**. **b**, **c**, **d**, **e**, and **f**, As in **a**, but for when intra-synaptic upscaling (β_{intra}) increases. Panel **d** here is as Fig. 1**d**. Shaded area and Error bar correspond to standard deviation over 500 trials.

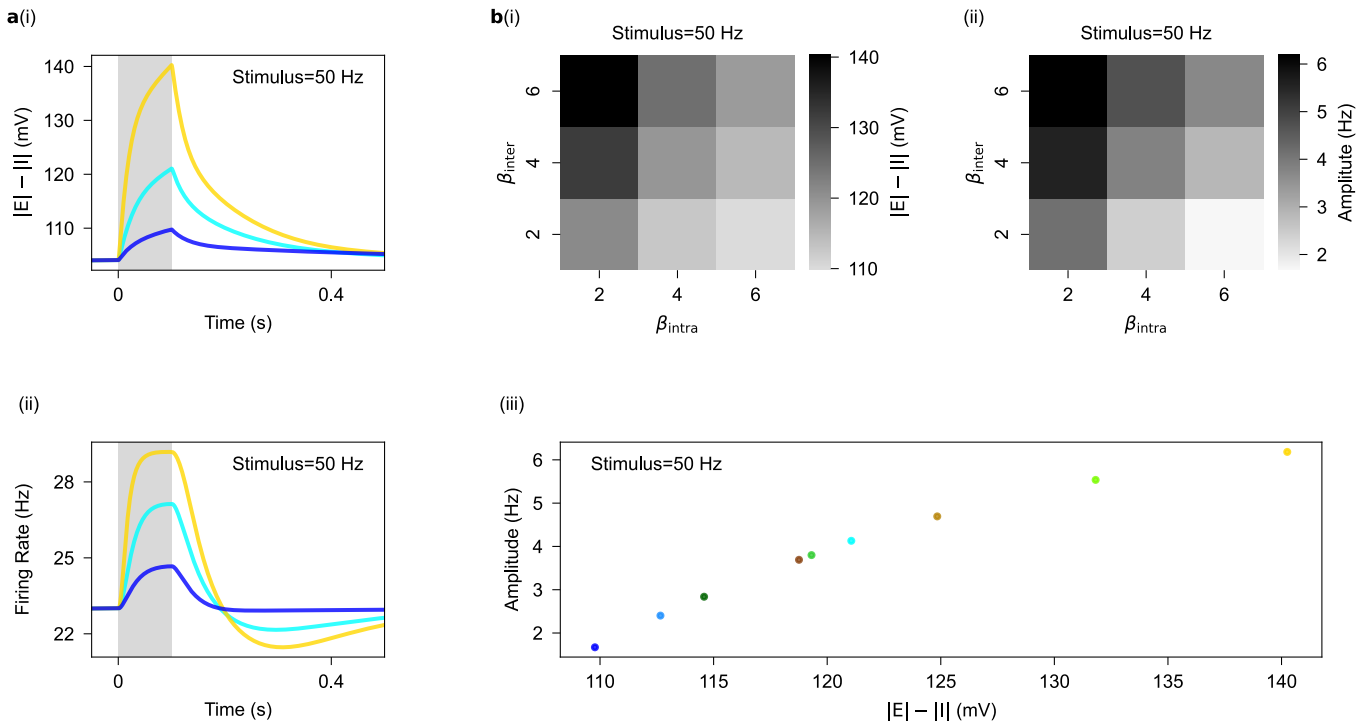

Extended Data Fig. 3. Effect of intra- and inter-synaptic upscaling on the net evoked synaptic current in the one-cortical-column model. a, The net evoked synaptic current (i), quantified as $|E| - |I|$, decreases with increasing β_{intra} (from ligh to dark blue) as opposed to when β_{inter} increases (from ligh blue to light yellow) in wakefulness. Changes in the time trace of net evoked synaptic currrent determine changes in the time trace of evoked firing responses (ii). This holds true for other values of stimulus intensity (not shown here). Note that the net synaptic current remains constant before stimulus onset across various synaptic upscaling scenarios, illustrating that synaptic upscaling is implemented in a balanced configuration without causing predominant excitation or inhibition. Shaded area corresponds to the stimulus duration. **b**, Effects of β_{intra} and β_{inter} on the net evoked synaptic currents explain the pulling and driving effects associated with the intra- and inter-synaptic upscalings in wakefulness. Intra-synaptic upscaling decreases the net evoked synaptic current (i) that results in the decreased evoked responses (ii). Conversely, inter-synaptic upscaling increases the net evoked synaptic current (i) that results in the increases evoked responses (ii). Changes in the net evoked synaptic currrent determine changes in the amplitude of evoked firing responses (iii). Note that analysis in **b** are carried out on the data points at stimulus offset.

DRAFT

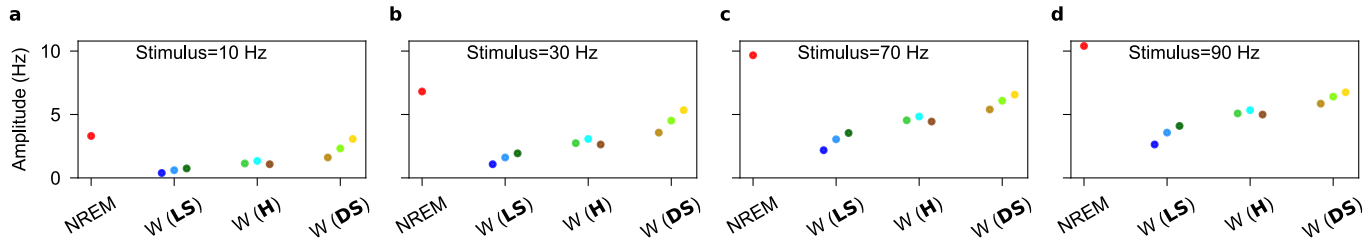

Extended Data Fig. 4. The amplitude of evoked firing responses in the one-cortical-column model. a, The amplitude of evoked firing responses increases with increasing values of synaptic upscaling ratio, $\beta_{inter}/\beta_{intra}$, during wakefulness when the stimulus intesity is 10 Hz (**a**), 30 Hz (**b**), 70 Hz (**c**) and 90 Hz (**d**). Note that the overall enhancement of the amplitude of evoked responses as the stimulus intesity increases from (**a**) to (**d**).

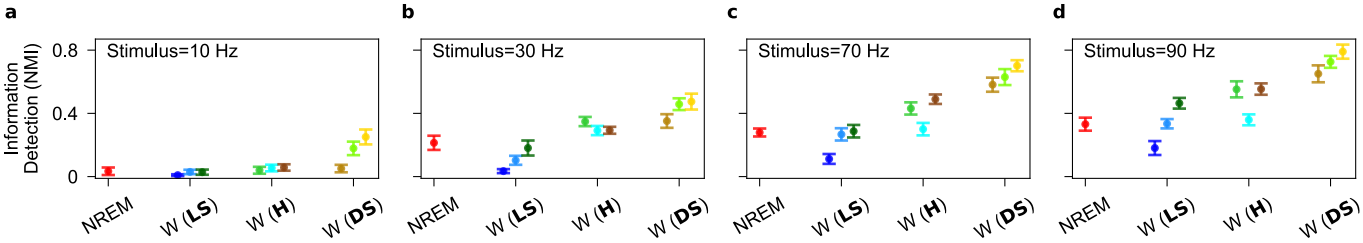

Extended Data Fig. 5. Information detection in the one-cortical-column model. a, Information detection increases with increasing values of synaptic upscaling ratio, $\beta_{\text{inter}}/\beta_{\text{intra}}$, during wakefulness when the stimulus intesity is 10 Hz (**a**), 30 Hz (**b**), 70 Hz (**c**) and 90 Hz (**d**). Synaptic upscaling during wakefulness does not enhance information detection during wakefulness across stimuli compared to those in NREM sleep unless it occurs in DS upscaling. Note that the overall enhancement of information detection as the stimulus intesity increases from (**a**) to (**d**). Error bar corresponds to 95% confidence interval over 10 performance estimate of the K-means clustering algorithms.

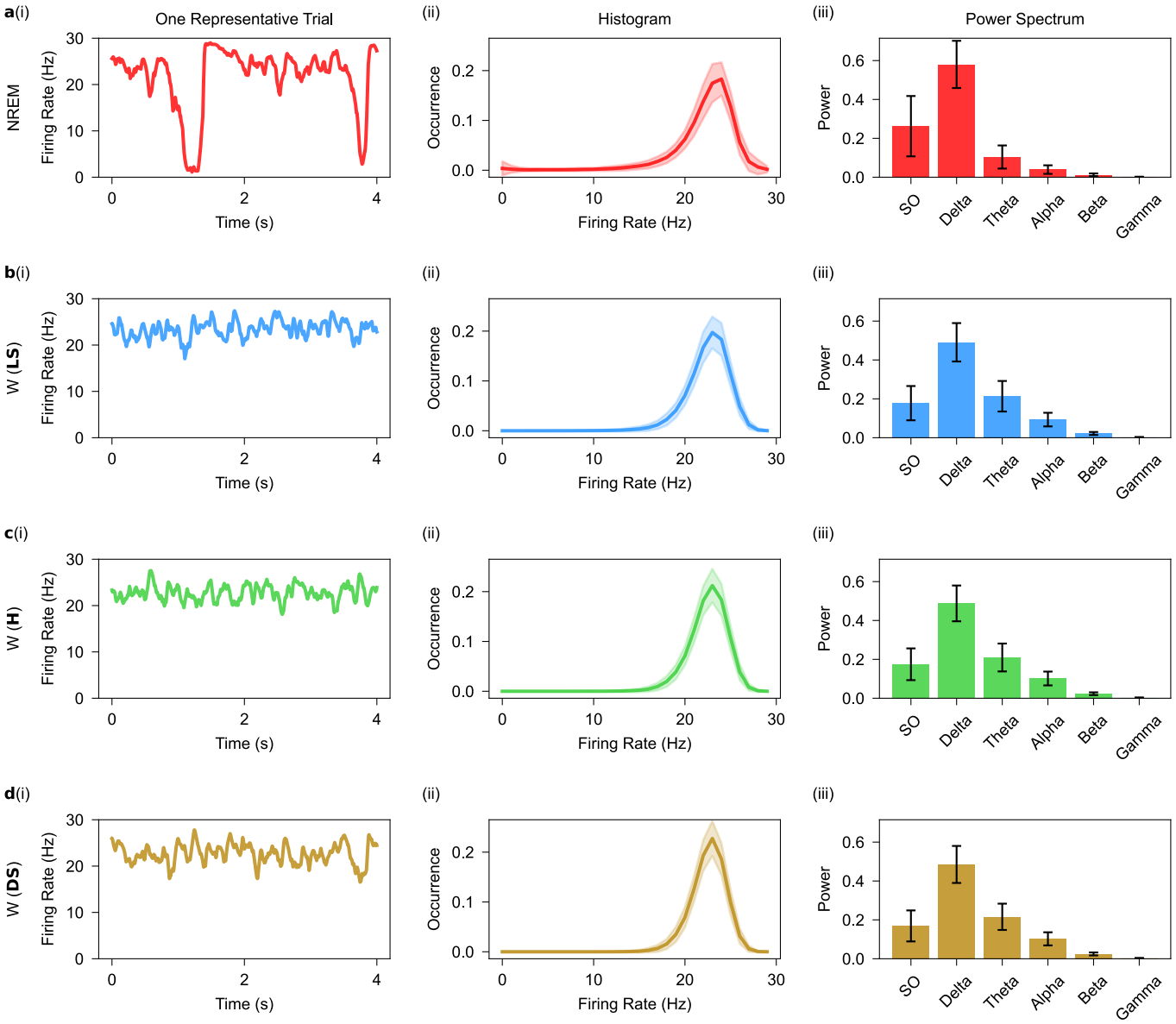

Extended Data Fig. 6. Dynamical features of spontaneous firing activity in the two-cortical-column model. a, Spontaneous firing rate signal for a representative trial (i), the distribution of firing rate signals (ii), and the power spectrum of signals (iii) when there is no intra-synaptic upscaling ($\beta_{\text{intra}} = 1$, $\beta_{\text{inter}} = 1$). **b**, **c**, and **d**, As in **a**, but for when synaptic upscaling is local-selective (LS: $\beta_{\text{intra}} = 4$, $\beta_{\text{inter}} = 2$), homogeneous (H: $\beta_{\text{intra}} = 4$, $\beta_{\text{inter}} = 4$), and distance-selective upscaling (DS: $\beta_{\text{intra}} = 4$, $\beta_{\text{inter}} = 6$), respectively. The dynamical features of spontaneous firing activity in the two-cortical-column model shift from NREM sleep to wakefulness for all synaptic upscaling combinations (not shown here). Shaded area and Error bar correspond to standard deviation over 500 trials.

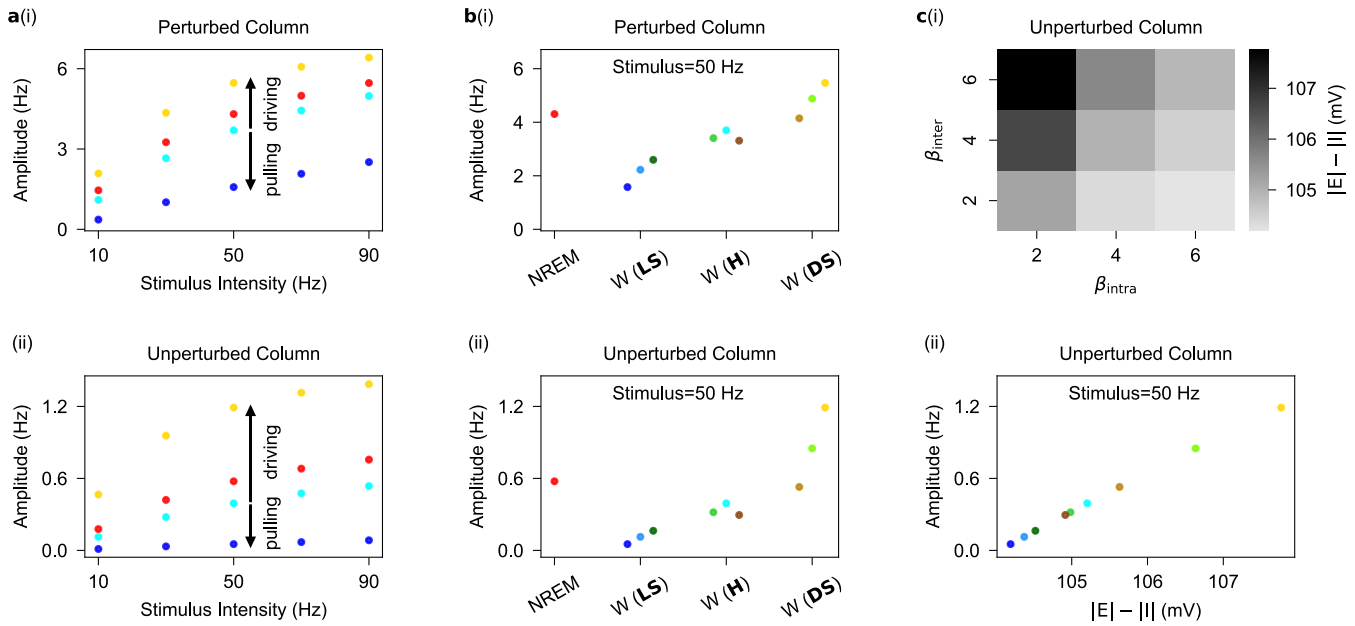

Extended Data Fig. 7. Effect of intra- and inter-synaptic upscaling on the response of two-cortical-column model to stimuli. **a**, Increasing intra-synaptic upscaling while inter-synaptic upscaling is constant from light to dark blue (from $\beta_{\text{intra}} = 2, \beta_{\text{inter}} = 2$ to $\beta_{\text{intra}} = 6, \beta_{\text{inter}} = 2$) during wakefulness produces a pulling effect on the amplitude of evoked firing responses in the perturbed (i) and unperturbed cortical column (ii). Conversely, increasing inter-synaptic upscaling while intra-synaptic upscaling is constant from light blue to light yellow (from $\beta_{\text{intra}} = 2, \beta_{\text{inter}} = 2$ to $\beta_{\text{intra}} = 2, \beta_{\text{inter}} = 6$) during wakefulness produces a driving effect on the amplitude of evoked firing responses in the perturbed (i) and unperturbed cortical column (ii). **b**, The amplitude of evoked firing responses increases as the synaptic upscaling transitions from local-selective (LS) to distance-selective (DS) upscaling during wakefulness in the perturbed (i) and unperturbed cortical column (ii). Note that this holds true for other values of stimulus intensity (not shown here). The amplitude of evoked responses to stimuli in the perturbed (i) and unperturbed cortical column (ii) during wakefulness enhances as synaptic upscaling transition from local-selective (LS) towards distance-selective (DS) upscaling. **c**, Inter-synaptic upscaling increases the net evoked synaptic current, as opposed to when intra-synaptic upscaling increases during wakefulness in the unperturbed cortical column (i). Changes in the net evoked synaptic currrent determine changes in the amplitude of evoked firing responses (ii).

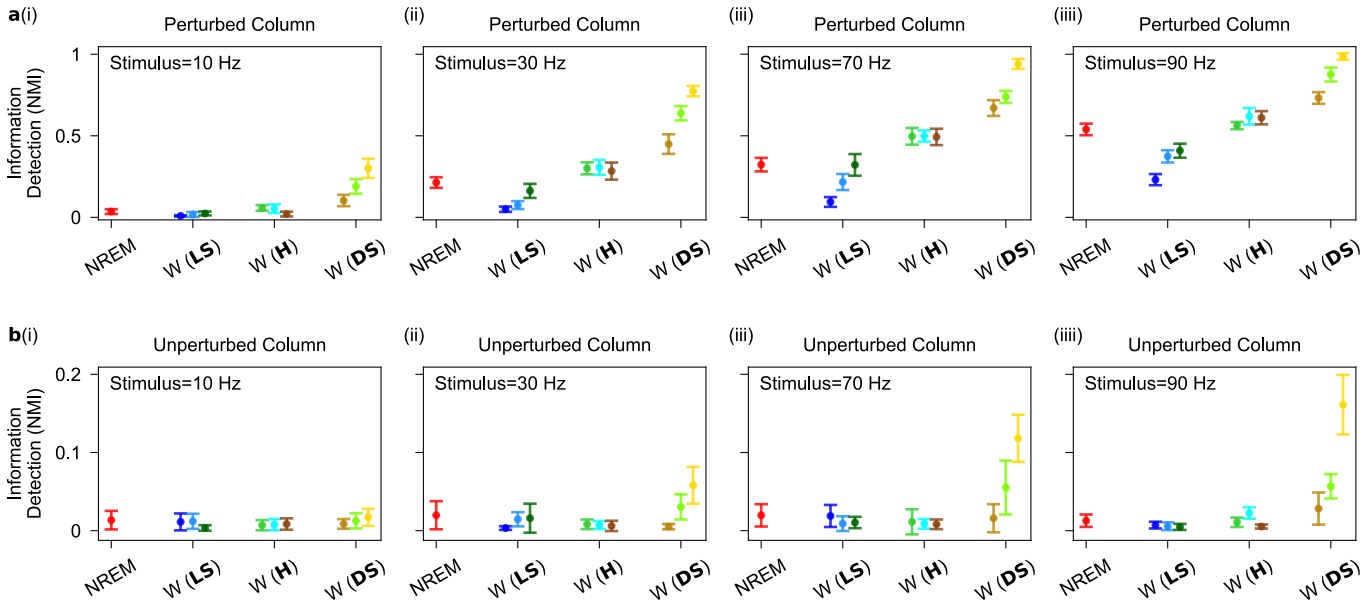

Extended Data Fig. 8. Information detection in the two-cortical-column model. **a**, Information detection increases with increasing values of synaptic upscaling ratio, $\beta_{\text{inter}}/\beta_{\text{intra}}$, during wakefulness when the stimulus intesity is 10 Hz (i), 30 Hz (ii), 70 Hz (iii) and 90 Hz (iiii). **b**, As in **a**, but for the unperturbed cortical column. Error bar corresponds to 95% confidence interval over 10 performance estimate of the K-means clustering algorithms.

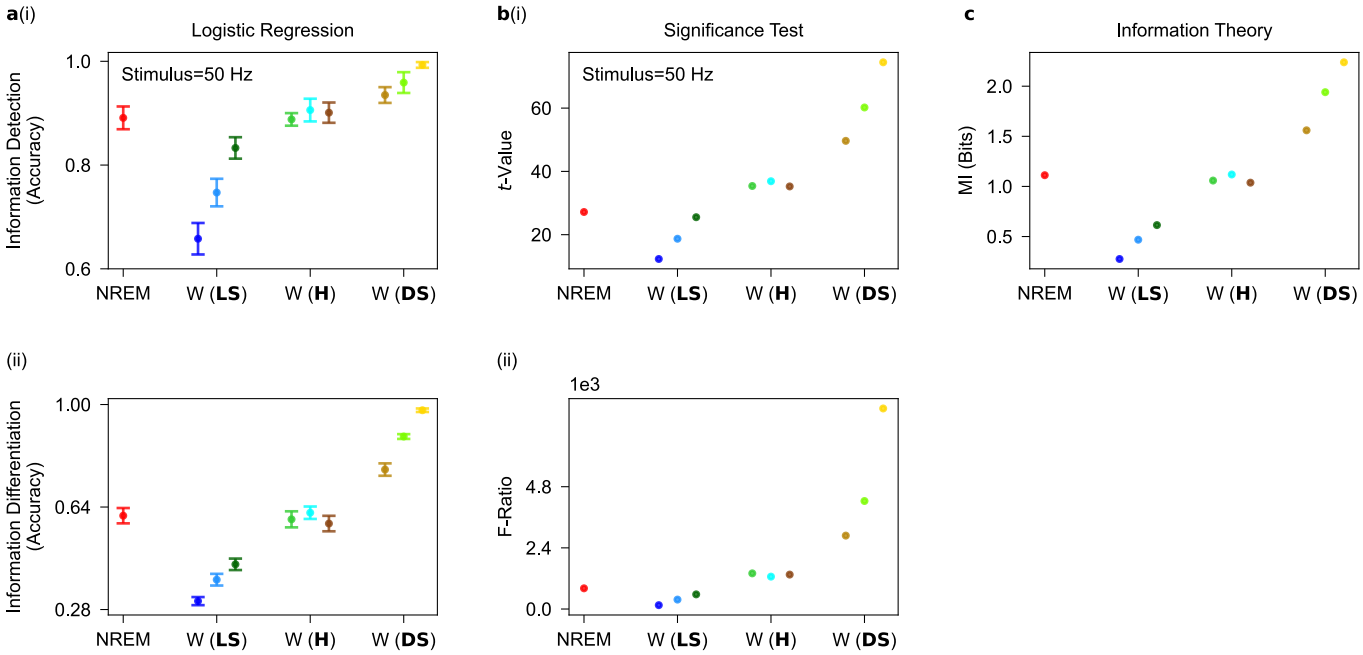

Extended Data Fig. 9. Robustness of the computational results. Figures pertain to analysis of evoked firing responses in the perturbed cortical column in the two-cortical-column model. **a**, Information detection for when stimulus intensity is 50Hz (i) and information differentiation (ii) when logistic classification algorithms (Methods) are employed. Error bar corresponds to 95% confidence interval over 10 performance estimate of the logistic classification algorithms. Logistic classification algorithms qualitatively replicate the results obtained using K-means clustering algorithms in Fig. 4**b**. **b**, Implementing significance tests (Methods) such as student t-test (i) and analysis of variance (ii) qualitatively replicate the results obtain by machine learning techniques pertaining to information detection and information differentiation. **c**, Implementing information theory (Methods) manifests that the mutual information between the distribution of evoked responses at stimulus offset and the distribution of stimuli increases as synaptic upscaling transitions from local-selective (LS) to distance-selective (DS) upscaling during wakefulness.

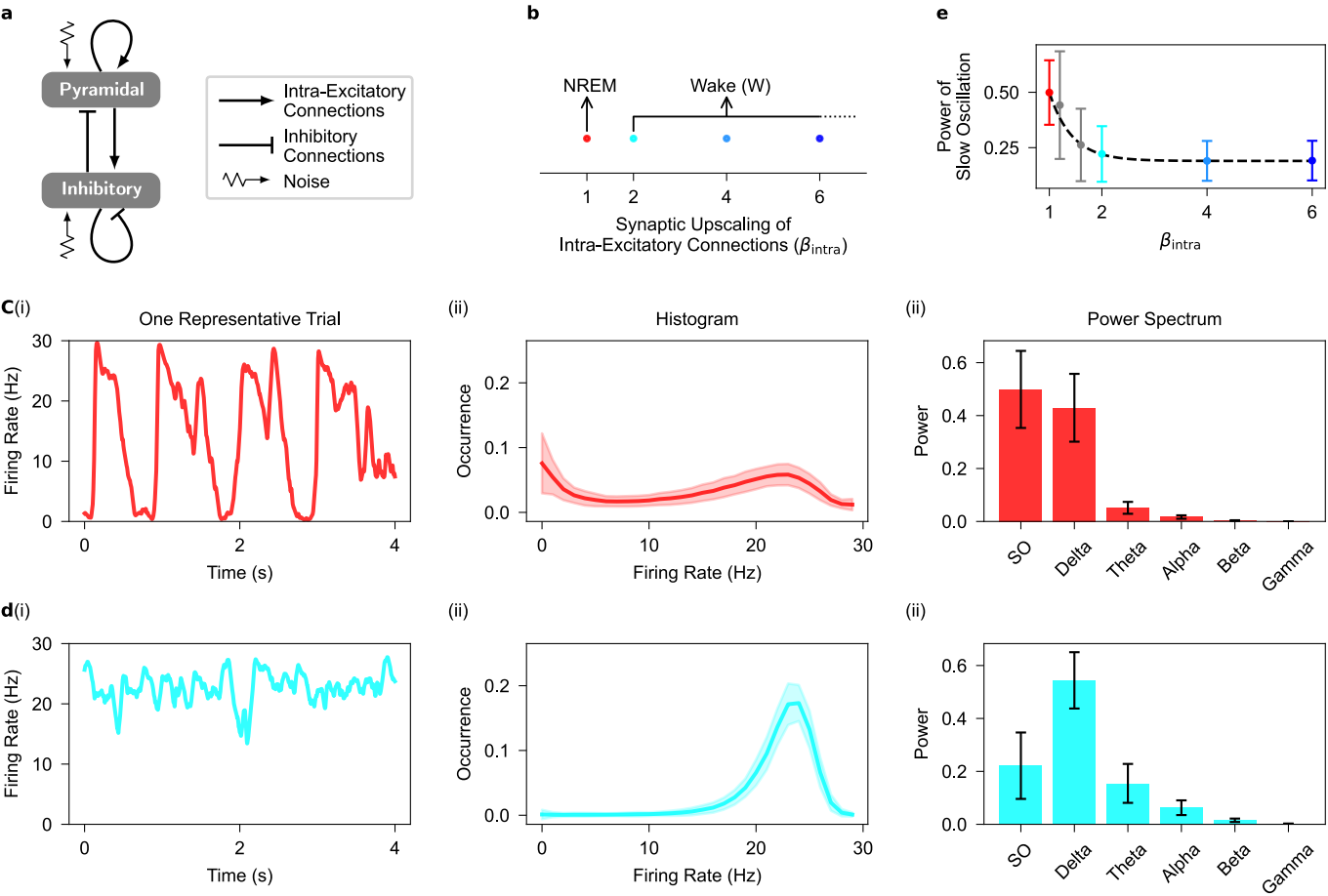
a
Pyramidal
Inhibitory
Intra-Excitatory Connections
Inhibitory Connections
Noise
b
NREM
Wake (W)
1
2
4
6
Synaptic Upscaling of Intra-Excitatory Connections (β_{intra})
e
Power of Slow Oscillation
0.50
0.25
1
2
4
6
β_{intra}
c(i)
One Representative Trial
Firing Rate (Hz)
Time (s)
(ii)
Histogram
Occurrence
Firing Rate (Hz)
(ii)
Power Spectrum
Power
SO
Delta
Theta
Alpha
Beta
Gamma
d(i)
Firing Rate (Hz)
Time (s)
(ii)
Occurrence
Firing Rate (Hz)
(ii)
Power
SO
Delta
Theta
Alpha
Beta
Gamma

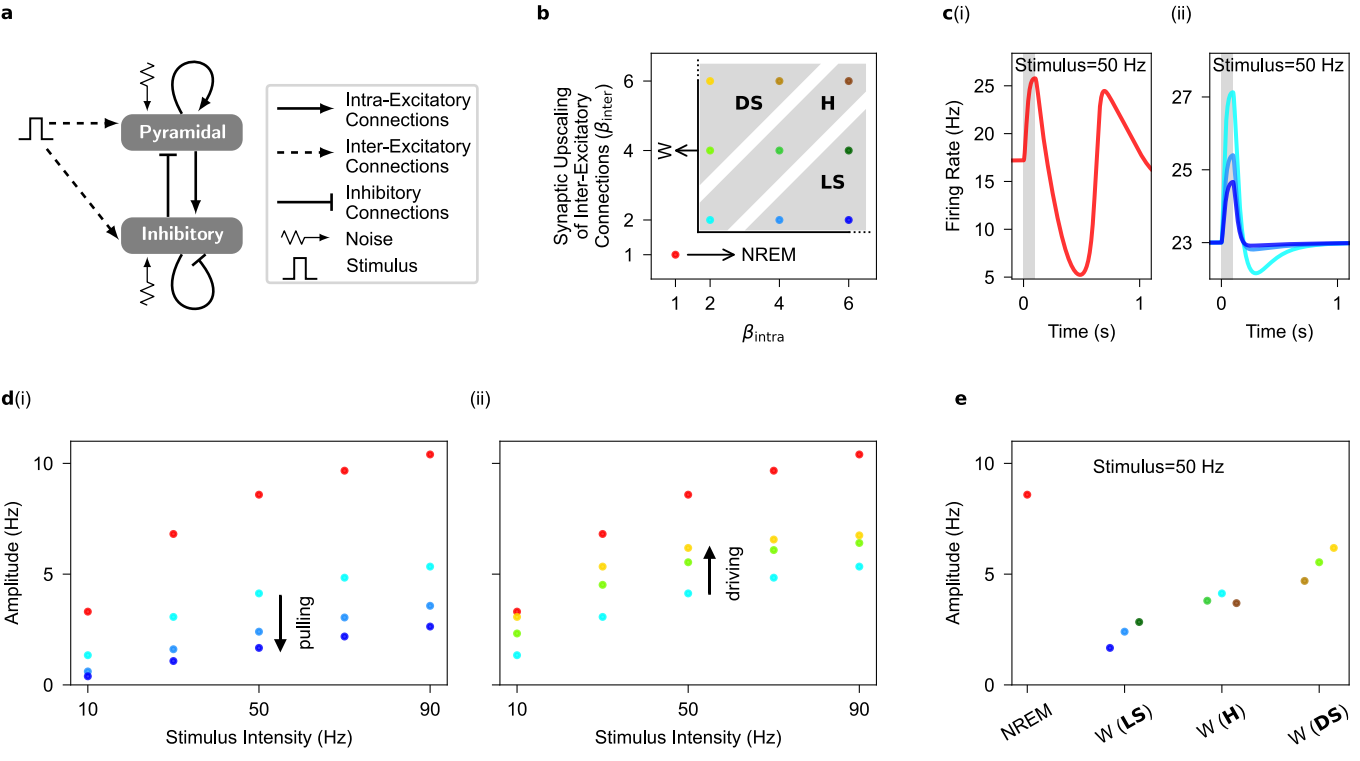
a
Pyramidal
Inhibitory
Intra-Excitatory Connections
Inter-Excitatory Connections
Inhibitory Connections
Noise
Stimulus
b
Synaptic Upscaling of Inter-Excitatory Connections (β_{inter})
β_{intra}
DS
H
LS
W
NREM
c(i)
(ii)
Stimulus=50 Hz
Firing Rate (Hz)
Time (s)
d(i)
(ii)
Amplitude (Hz)
Stimulus Intensity (Hz)
pulling
driving
e
Stimulus=50 Hz
Amplitude (Hz)
NREM
W (LS)
W (H)
W (DS)

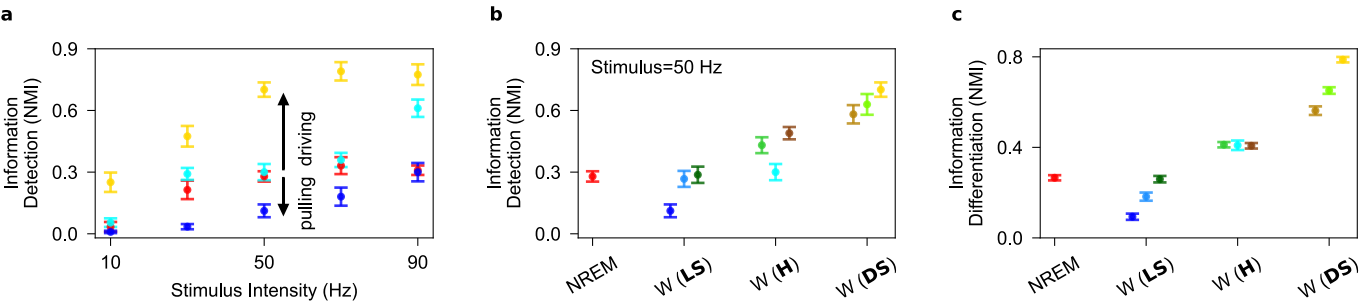
a
Information Detection (NMI)
0.9
0.6
0.3
0.0
10
50
90
Stimulus Intensity (Hz)
pulling
driving
b
Information Detection (NMI)
Stimulus=50 Hz
NREM
W (LS)
W (H)
W (DS)
c
Information Differentiation (NMI)
0.8
0.4
0.0

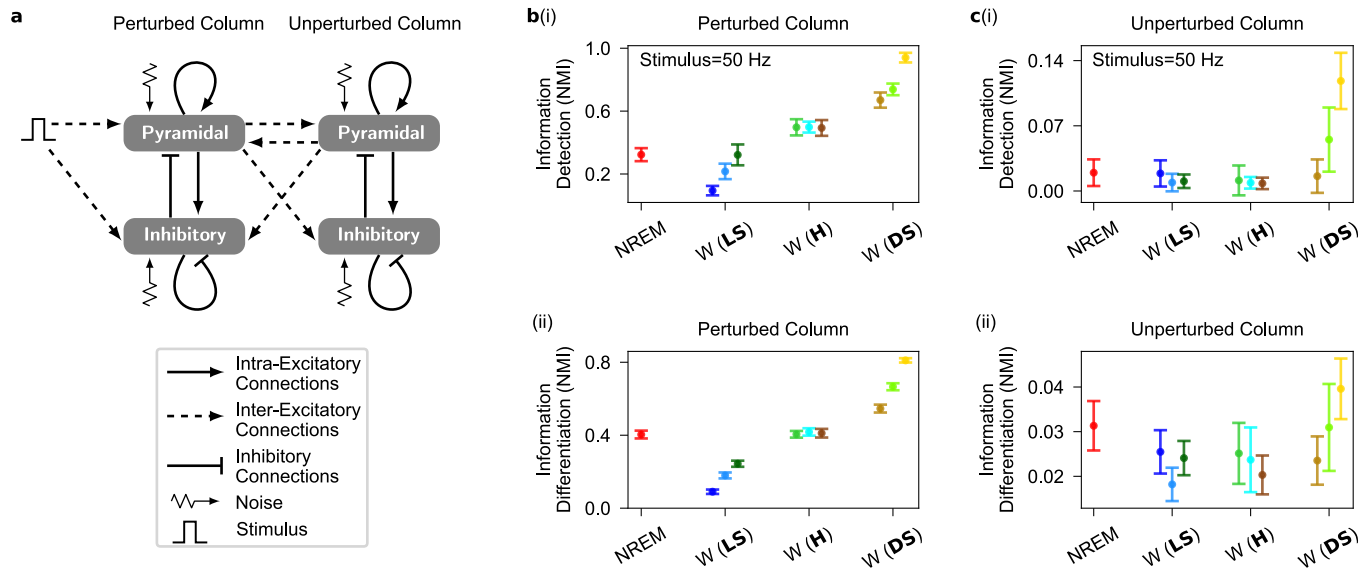
a
Perturbed Column
Unperturbed Column
Pyramidal
Pyramidal
Inhibitory
Inhibitory
Intra-Excitatory Connections
Inter-Excitatory Connections
Inhibitory Connections
Noise
Stimulus
b(i)
Perturbed Column
Stimulus=50 Hz
Information Detection (NMI)
1.0
0.6
0.2
NREM
W (LS)
W (H)
W (DS)
c(i)
Unperturbed Column
Stimulus=50 Hz
Information Detection (NMI)
0.14
0.07
0.00
NREM
W (LS)
W (H)
W (DS)
(ii)
Perturbed Column
Information Differentiation (NMI)
0.8
0.4
0.0
NREM
W (LS)
W (H)
W (DS)
(ii)
Unperturbed Column
Information Differentiation (NMI)
0.04
0.03
0.02
NREM
W (LS)
W (H)
W (DS)

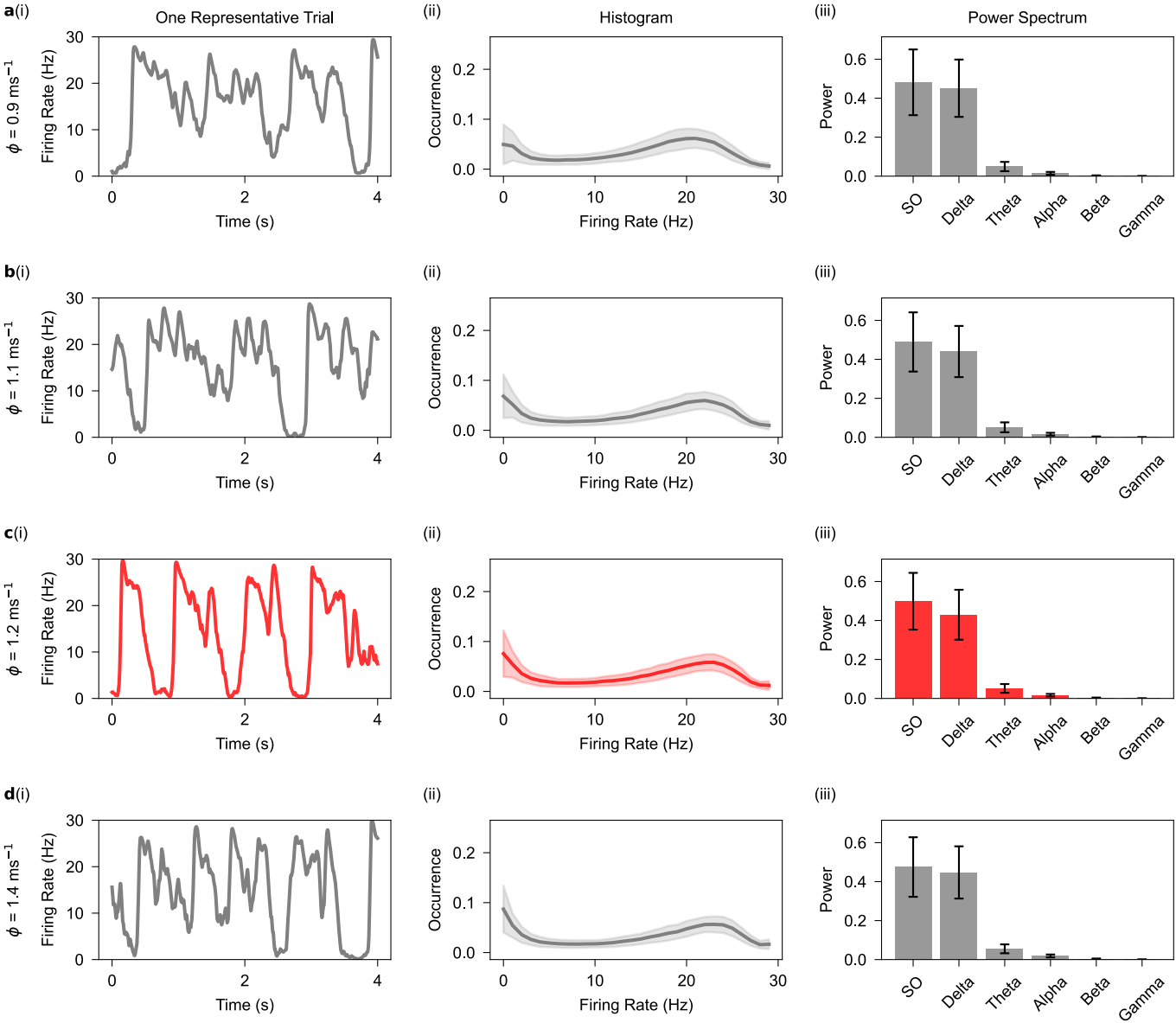
a(i)
One Representative Trial
(ii)
Histogram
(iii)
Power Spectrum
ϕ = 0.9 ms⁻¹
ϕ = 1.1 ms⁻¹
ϕ = 1.2 ms⁻¹
ϕ = 1.4 ms⁻¹
b(i)
c(i)
d(i)
Firing Rate (Hz)
Time (s)
Occurrence
Firing Rate (Hz)
Power
SO
Delta
Theta
Alpha
Beta
Gamma

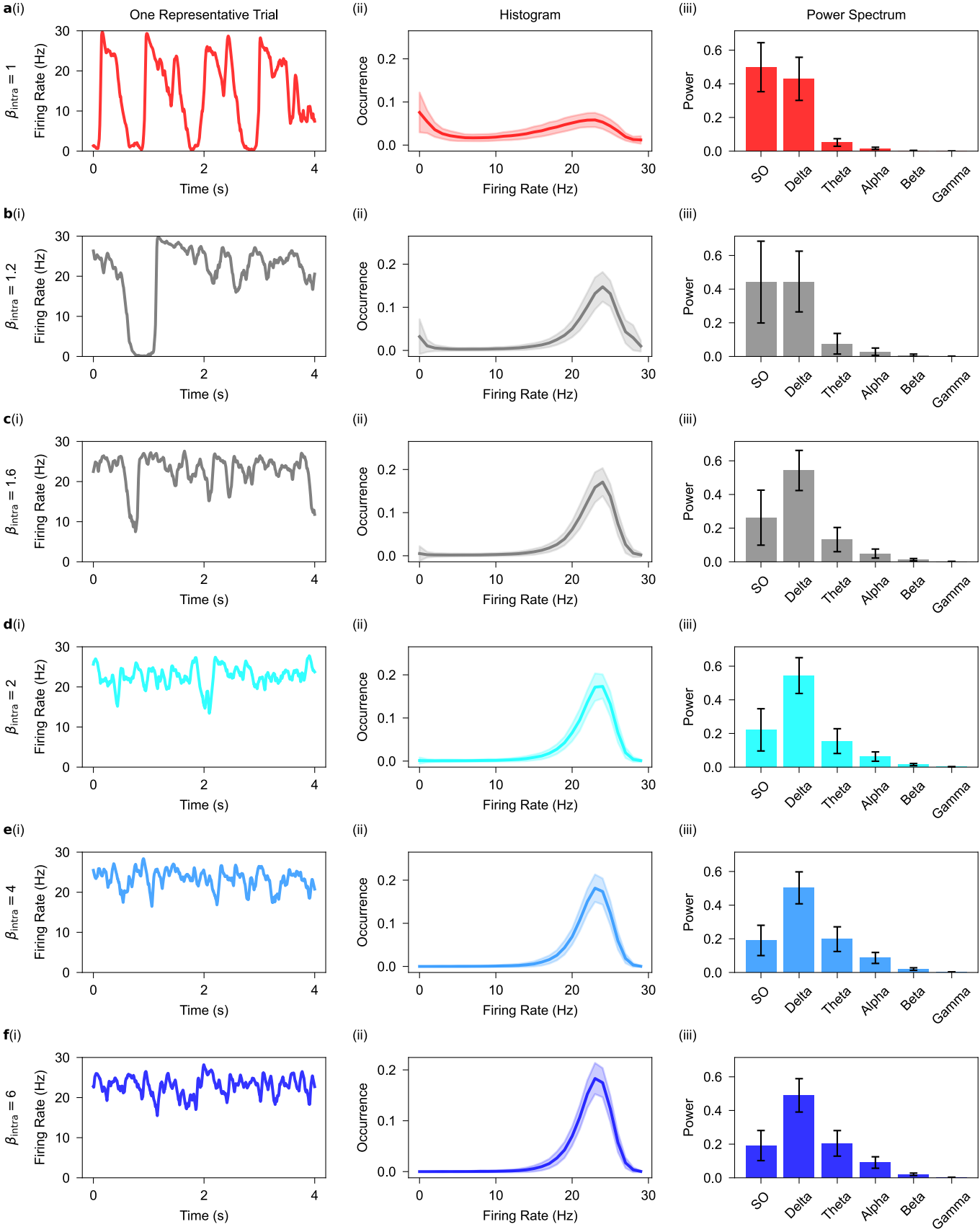
a(i)
One Representative Trial
(ii)
Histogram
(iii)
Power Spectrum
$\beta_{intra} = 1$
$\beta_{intra} = 1.2$
$\beta_{intra} = 1.6$
$\beta_{intra} = 2$
$\beta_{intra} = 4$
$\beta_{intra} = 6$
b(i)
c(i)
d(i)
e(i)
f(i)
Firing Rate (Hz)
Time (s)
Occurrence
Power
SO
Delta
Theta
Alpha
Beta
Gamma

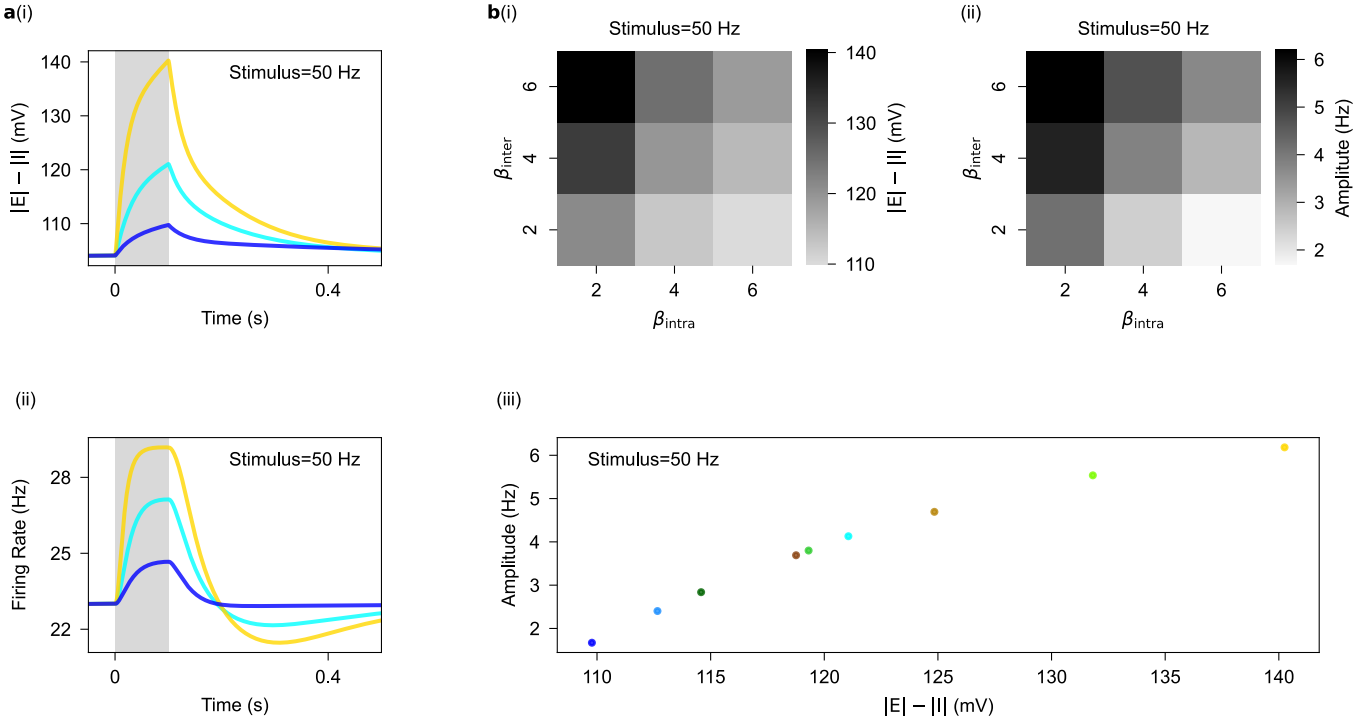
a(i)
Stimulus=50 Hz
|E| − |I| (mV)
140
130
120
110
0
0.4
Time (s)
b(i)
Stimulus=50 Hz
β_{inter}
β_{intra}
|E| − |I| (mV)
(ii)
Stimulus=50 Hz
Amplitude (Hz)
(ii)
Stimulus=50 Hz
Firing Rate (Hz)
28
25
22
Time (s)
(iii)
Stimulus=50 Hz
Amplitude (Hz)
|E| − |I| (mV)

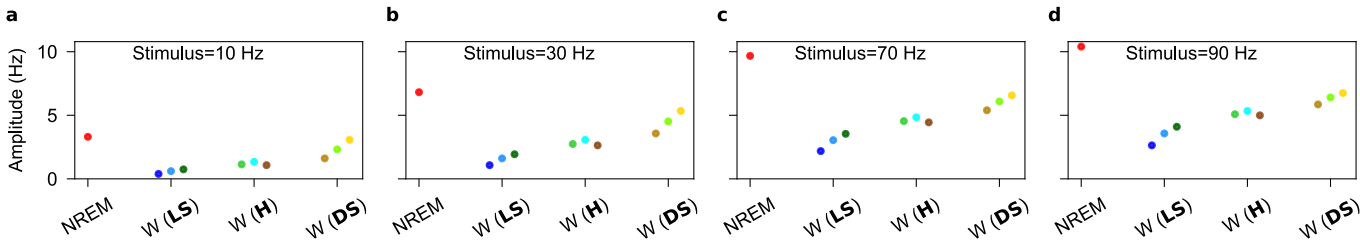
a
b
c
d
Amplitude (Hz)
10
5
0
Stimulus=10 Hz
Stimulus=30 Hz
Stimulus=70 Hz
Stimulus=90 Hz
NREM
W (LS)
W (H)
W (DS)

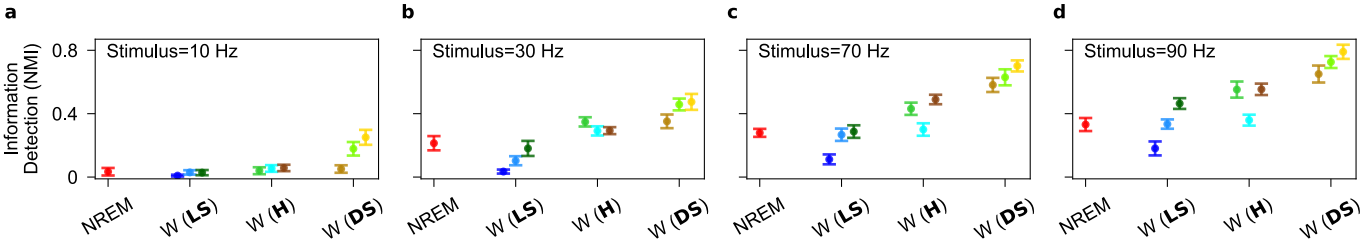
a
b
c
d
Information Detection (NMI)
0.8
0.4
0
Stimulus=10 Hz
Stimulus=30 Hz
Stimulus=70 Hz
Stimulus=90 Hz
NREM
W (LS)
W (H)
W (DS)

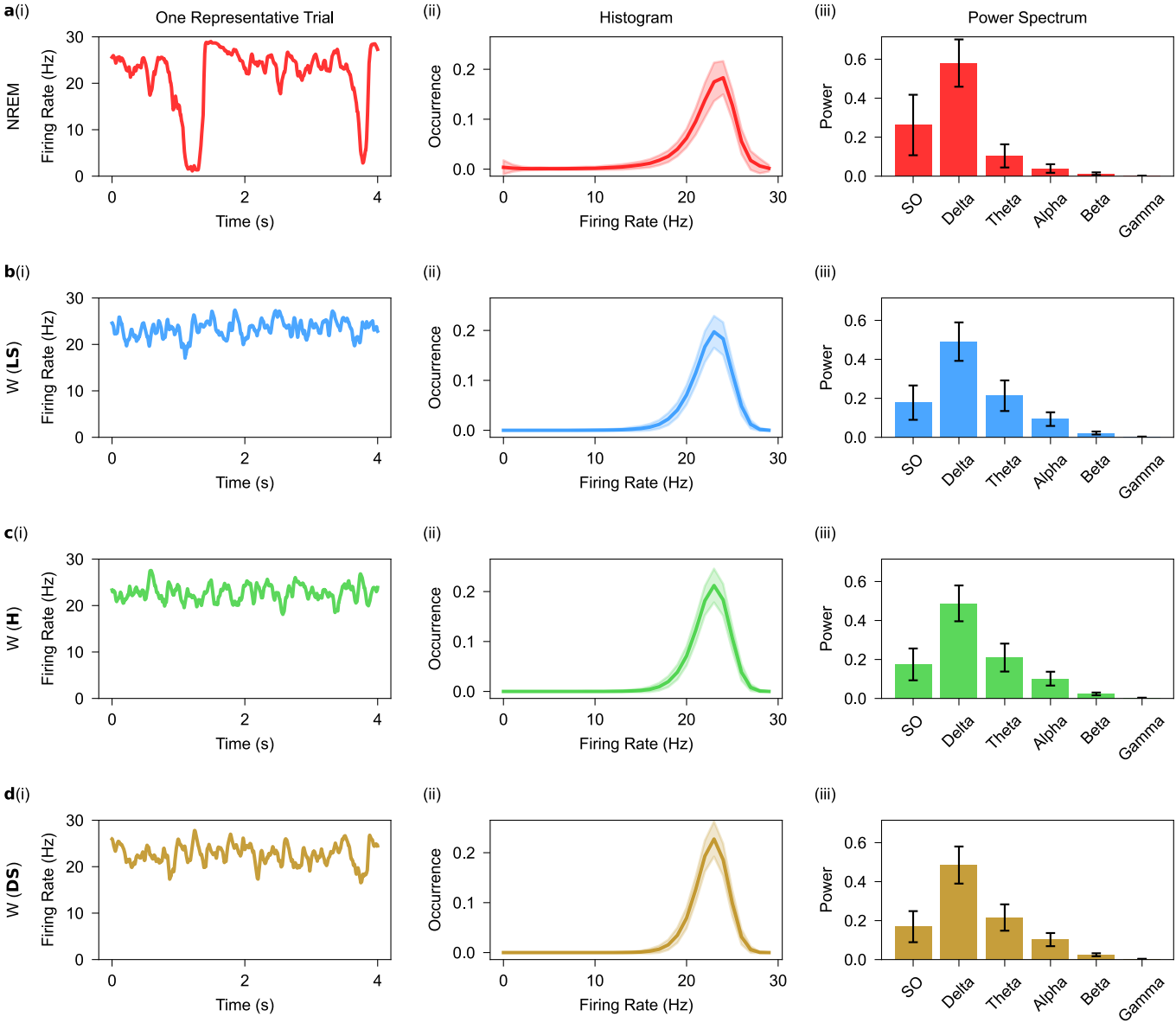
a(i)
One Representative Trial
NREM
Firing Rate (Hz)
Time (s)
(ii)
Histogram
Occurrence
Firing Rate (Hz)
(iii)
Power Spectrum
Power
SO
Delta
Theta
Alpha
Beta
Gamma
b(i)
W (LS)
c(i)
W (H)
d(i)
W (DS)

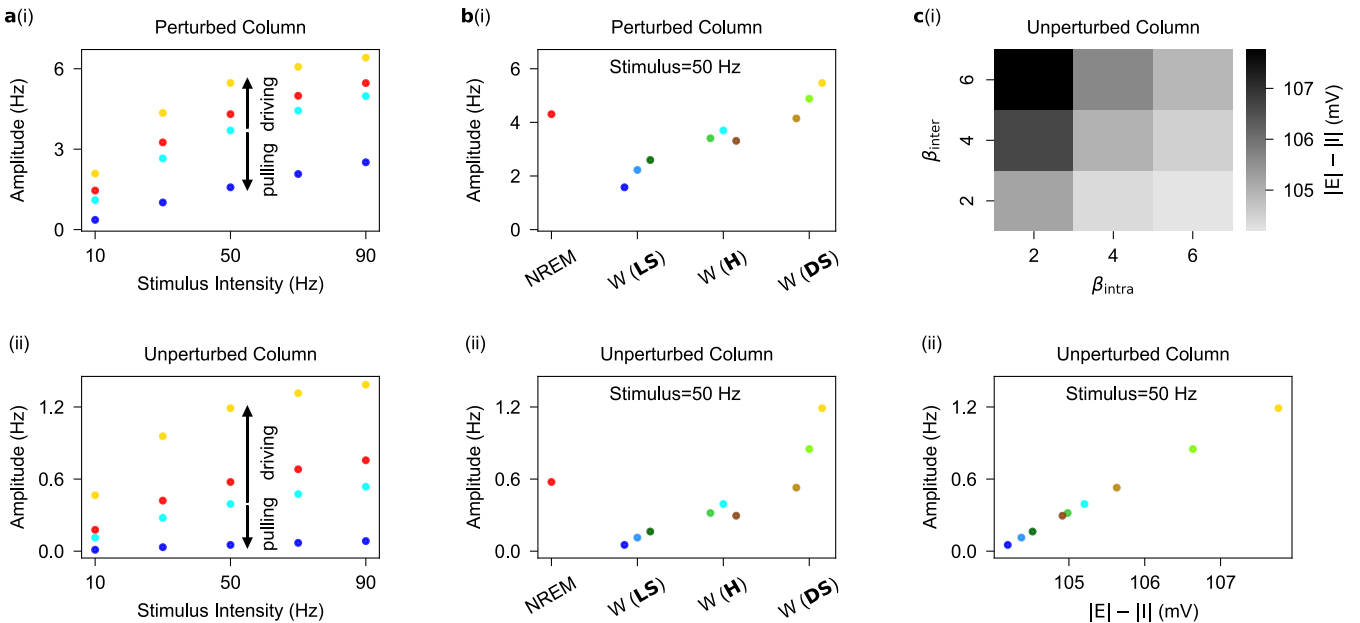
a(i)
Perturbed Column
Amplitude (Hz)
Stimulus Intensity (Hz)
driving
pulling
b(i)
Perturbed Column
Stimulus=50 Hz
Amplitude (Hz)
NREM
W (LS)
W (H)
W (DS)
c(i)
Unperturbed Column
β_{inter}
β_{intra}
|E| − |I| (mV)
(ii)
Unperturbed Column
Amplitude (Hz)
Stimulus Intensity (Hz)
driving
pulling
(ii)
Unperturbed Column
Stimulus=50 Hz
Amplitude (Hz)
NREM
W (LS)
W (H)
W (DS)
(ii)
Unperturbed Column
Stimulus=50 Hz
Amplitude (Hz)
|E| − |I| (mV)

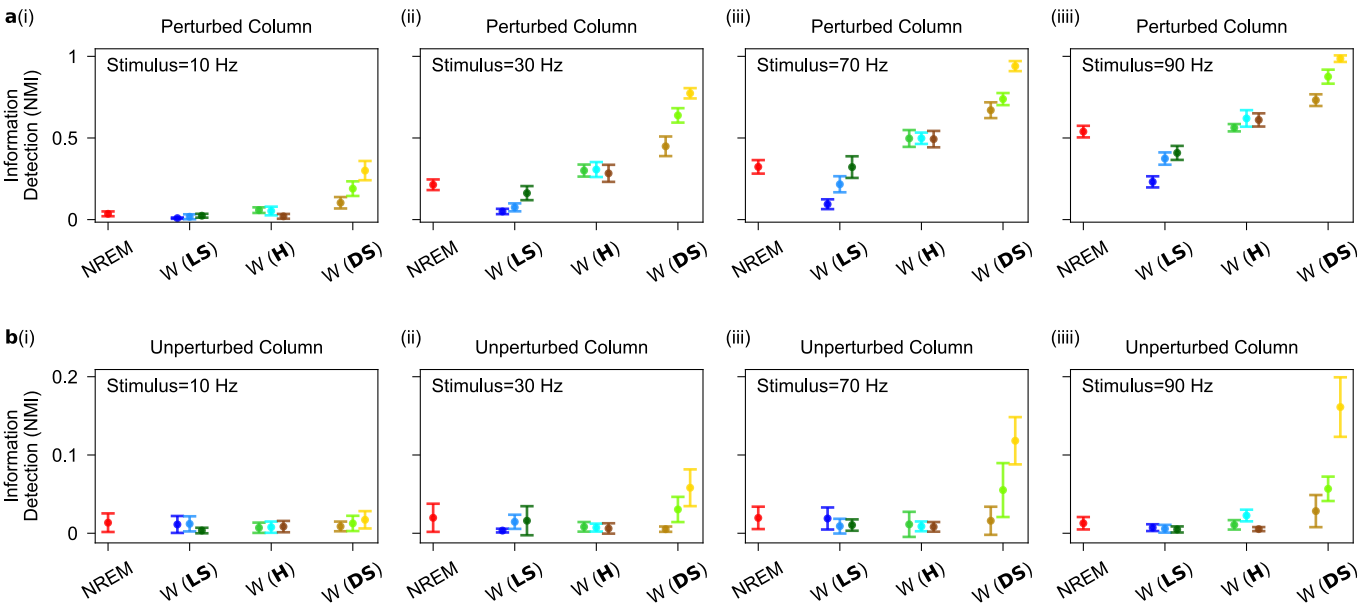
a(i)
Perturbed Column
Stimulus=10 Hz
(ii)
Perturbed Column
Stimulus=30 Hz
(iii)
Perturbed Column
Stimulus=70 Hz
(iiii)
Perturbed Column
Stimulus=90 Hz
Information Detection (NMI)
1
0.5
0
NREM
W (LS)
W (H)
W (DS)
b(i)
Unperturbed Column
Stimulus=10 Hz
(ii)
Unperturbed Column
Stimulus=30 Hz
(iii)
Unperturbed Column
Stimulus=70 Hz
(iiii)
Unperturbed Column
Stimulus=90 Hz
Information Detection (NMI)
0.2
0.1
0
NREM
W (LS)
W (H)
W (DS)

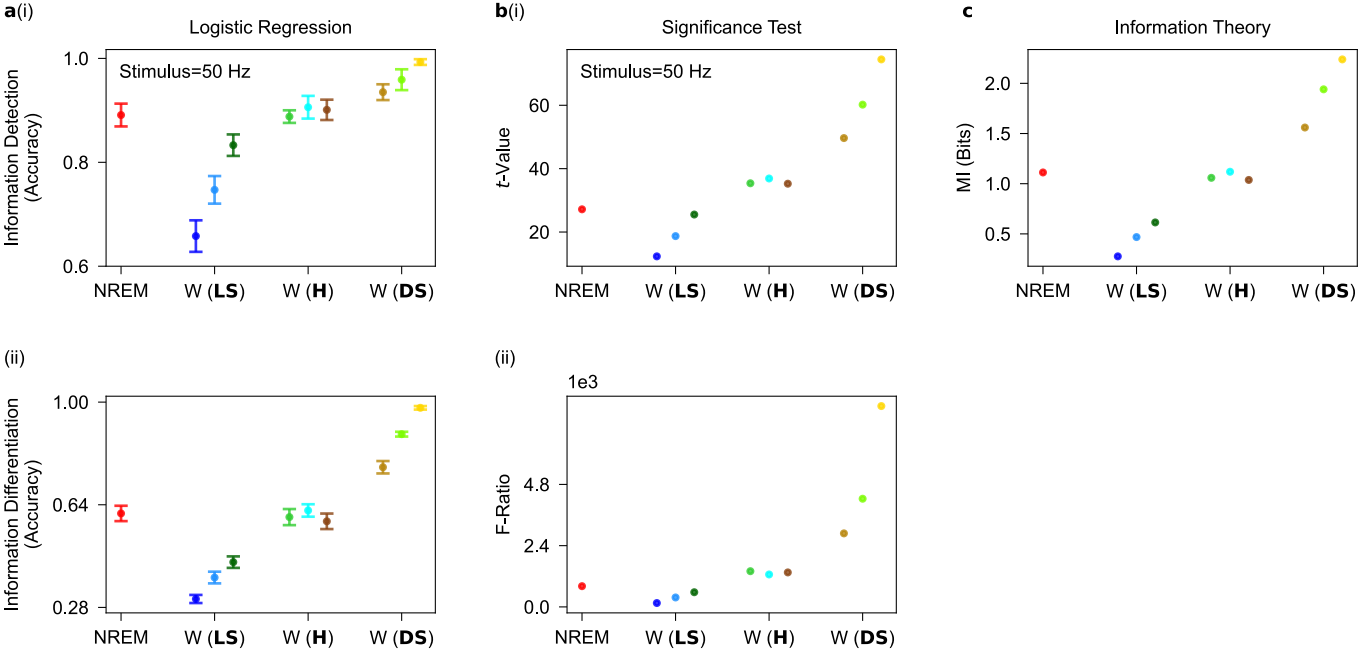
a(i)
Logistic Regression
Stimulus=50 Hz
Information Detection (Accuracy)
1.0
0.8
0.6
NREM
W (LS)
W (H)
W (DS)
b(i)
Significance Test
Stimulus=50 Hz
t-Value
60
40
20
c
Information Theory
MI (Bits)
2.0
1.5
1.0
0.5
(ii)
Information Differentiation (Accuracy)
1.00
0.64
0.28
(ii)
1e3
F-Ratio
4.8
2.4
0.0